UCRL-ID-139906

Uncertainty Budget and Efficiency Analysis for the ^{239}Pu($n,2n\Upsilon$) Partial Reaction Cross-Section Measurements

D.P. McNabb, D.E. Archer, J.A. Becker, L.A. Bernstein, P.E. Garrett, K. Hauschild, C.A. McGrath, W. Younes, M. Devlin, D.M. Drake, G.D. Johns, R.O. Nelson, W.S. Wilburn

May 1, 2000

DISCLAIMER

This document was prepared as an account of work sponsored by an agency of the United States Government. Neither the United States Government nor the University of California nor any of their employees, makes any warranty, express or implied, or assumes any legal liability or responsibility for the accuracy, completeness, or usefulness of any information, apparatus, product, or process disclosed, or represents that its use would not infringe privately owned rights. Reference herein to any specific commercial product, process, or service by trade name, trademark, manufacturer, or otherwise, does not necessarily constitute or imply its endorsement, recommendation, or favoring by the United States Government or the University of California. The views and opinions of authors expressed herein do not necessarily state or reflect those of the United States Government or the University of California, and shall not be used for advertising or product endorsement purposes.

This work was performed under the auspices of the U. S. Department of Energy by the University of California, Lawrence Livermore National Laboratory under Contract No. W-7405-Eng-48.

This report has been reproduced
directly from the best available copy.

Available to DOE and DOE contractors from the
Office of Scientific and Technical Information
P.O. Box 62, Oak Ridge, TN 37831
Prices available from (423) 576-8401
http://apollo.osti.gov/bridge/

Available to the public from the
National Technical Information Service
U.S. Department of Commerce
5285 Port Royal Rd.,
Springfield, VA 22161
http://www.ntis.gov/

OR

Lawrence Livermore National Laboratory
Technical Information Department's Digital Library
http://www.llnl.gov/tid/Library.html

Uncertainty budget and efficiency analysis for the ^{239}Pu(n,$2n\gamma$) partial reaction cross-section measurements

D. P. McNabb, D. E. Archer, J. A. Becker, L. A. Bernstein, P. E. Garrett, K. Hauschild, C. A. McGrath, W. Younes

LLNL

M. Devlin, D. M. Drake, G. D. Johns, R. O. Nelson, W. S. Wilburn

LANL

The data and analysis in this report is current as of May 1, 2000

Contents

1   Introduction

The ^{239}Pu$(n,2n\gamma)^{238}$Pu partial reaction cross-section, $\sigma_{(n,2n\gamma)}$, has been measured as a function of neutron energy for several transitions in ^{238}Pu. Partial γ-ray cross sections for yrast, "collector" transitions, can provide especially valuable constraints on the magnitude and shape of the total $(n,2n)$ reaction cross-section. In essence, nuclear reaction models will be used to infer the shape and magnitude of the total $(n,2n)$ reaction cross-section from the measured partial γ-ray cross-sections.

The reason for undertaking this somewhat indirect approach is that previous measurements of the ^{239}Pu$(n,2n\gamma)$ have been hampered by a variety of constraints. Activation measurements have several hurdles: (1) intense flux and long counting times are required to overcome the relatively long half-life of ^{238}Pu (87 years) and (2) isotopically pure samples of ^{239}Pu in an environment free of ^{238}Pu contamination are difficult to come by. Neutron counting experiments are subject to significant uncertainties because (1) large background statistics from fission neutrons and (2) the experimental fission neutron multiplicity spectrum is subject to systematic errors because the flux of low-energy neutrons which induce fissions in thermally-fissile ^{239}Pu is very difficult to characterize.

In this measurement, spallation neutrons are provided by the LANSCE/WNR facility, and reaction neutron energies are determined via time-of-flight. Neutron flux is monitored in-beam with one ^{235}U fission chamber and one ^{238}U fission chamber. The ^{238}U is not sensitive to background from low-energy neutrons, whereas the ^{235}U fission chamber has better statistics. Hence, in essence the partial γ-ray cross sections are normalized to the evaluated fission cross sections of ^{235}U and ^{238}U. As a check of our normalization to provide additional constraints to the nuclear reaction modeling, benchmark measurements of ^{nat}Fe$(n,n'\gamma)$ and ^{235}U$(n,2n\gamma)$ have also been undertaken.

The secondary γ-rays are measured with the GEANIE array. GEANIE consists of eleven Compton-suppressed planar detectors, nine suppressed and six unsuppressed co-axial detectors.

Any absolute cross section measurement requires a complete understanding of array performance, flux normalization, and target effects. Important items to consider in this experiment include intrinsic detector efficiency, beam and detector geometry corrections, target attenuation, and deadtime. Radioactive targets give rise to significant counting rates in the GEANIE array resulting a large deadtime. The magnitude, energy dependence, and uncertainties of these effects and other corrections are the subject of this paper.

Figure 1 shows the yrast (lowest energy state for a given J^π) rotational levels and E2 transition energies in ^{238}Pu. Generally, the lower spin transitions are better collectors, but in actinide nuclei also have progressively larger internal conversion decay branches. The maximum γ-ray statistics usually occurs for the $6^+ \rightarrow 4^+$ transition. In an experiment at neutron energy, E_n, the number of γ rays emitted for a particular $(n,2n\gamma)$ transition is given by

$$N_{\gamma_{emit}} = \Phi \left(\frac{\rho l N_A}{A} \right) \left(\frac{1}{1+\alpha} \right) \sigma_{(n,2n\gamma)} \tag{1}$$
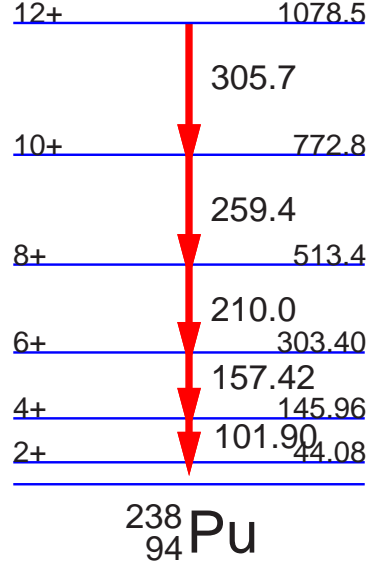
Figure 1: Lowest-lying yrast levels and γ-ray transition energies in ^{238}Pu. The J^π values for each level are given on the left, and the level energies in keV are listed on the right. Thre transition energies are also given in keV.

where

$$\Phi = \text{Number of neutrons in energy bin} \qquad (2)$$

$$\rho = \text{Mass density of } ^{239}\text{Pu in target} \qquad (3)$$

$$l = \text{Target thickness} \qquad (4)$$

$$N_A = 6.02205 \times 10^{23}/\text{mole} \qquad (5)$$

$$A = 239.052 \text{ gram/mole} \cdot \text{atom} \qquad (6)$$

$$\alpha = \text{Electron internal conversion coefficient} \qquad (7)$$

Not all emitted γ rays are observed because (1) only some fraction, $\frac{N_{\gamma emit}}{N_{\gamma escape}}$ of emitted γ rays are not attenuated in the target, and (2) the geometrical and intrinsic efficiency of the GEANIE array for measuring the full energy of the γ ray, ε, is only about 5%. Accounting for these two effects, the reaction cross-section is given by

$$\sigma_{(n,2n\gamma)} = \left(\frac{N_{\gamma obs}}{\Phi}\right)\left(\frac{A}{\rho l N_A}\right)\left(\frac{N_{\gamma emit}}{N_{\gamma escape}}\right)\left(\frac{1}{\varepsilon}\right)\left(1 + \alpha\right) \qquad (8)$$

There are five terms in Eq. 8, which are considered in turn along with relevant uncertainties in the following sections. These sections include

Sect. 2: Observed γ rays and neutron flux The discussion is broken into two parts: (1) the number of observed γ-rays in the collector transitions and (2) determination of the

neutron flux from the number of observed events in the fission chambers used to monitor flux.

Sect. 3: Target areal density The results of three approaches to determining the target areal density are presented.

Sect. 4: Absolute peak efficiency for a point source The measurement of the absolute peak efficiency for a point source is presented with a discussion of geometric and intrinsic effects. Special attention given to the method of deadtime corrections. An MCNP model of the array is presented and used to interpolate the efficiency between measured energies.

Sect. 5: Correction to efficiency for extended beam spot geometry The MCNP model is used to determine the efficiency for the extended beam spot source. Validation and verification of this approach is discussed.

Sect. 6: Attenuation effects Discussion of γ-ray attenuation in target as determined from closed-form calculation and validated with MCNP calculations. Several tests of this procedure were performed.

Sect. 7: Internal conversion coefficients Calculations of internal conversion coefficients are compared with experiments in the actinide mass region in order to estimate the uncertainty of the calculations.

The conclusion contains a summary of the important points, and a summary of the current state of the error budget in tabular form.

2 Observed γ rays and neutron flux

The neutron energy is measured via time of flight. The proton pulses that generate spallation neutrons in the primary target also generate photons. These prompt photons serve as the reference point for determining the neutron time of flight. Each time-of-flight bin corresponds to a particular energy bin. The number of neutrons incident on the target in each energy bin, $\Phi(E_n)$, must be known in order to normalize the γ-ray counts properly in Eq. 8. A subtle point is that the spatial distribution of neutrons must also be well understood. As discussed in Section 5, the probability of detecting a γ-ray depends upon its location in the target when it is emitted. However, the target is smaller than the neutron flux monitor and the neutron beam profile does not extend beyond the target in any significant amount, so the number of neutrons incident on the neutron flux monitor is equal to the number of neutrons incident on the target. Neutron scattering in the fission chamber and the intervening air can be ignored.

2.1 Observed γs

The observed γ-ray counts are histogrammed off-line to generate a γ-ray spectrum. The software and hardware conditions that determine the resulting spectrum are discussed in [You00]. The γ-ray line shapes must be characterized for each spectrum in order to distinguish background from photopeak counts. Depending on background and the local density of γ-ray lines, determining the counts in a particular transition can range from a simple sum of counts to a sophisticated maximum likelihood analysis. The details of this analysis varies from experiment to experiment, and is discussed for the ^{239}Pu$(n,2n\gamma)$ measurement in [Ber00] and for the ^{235}U$(n,2n\gamma)$ measurement in [You00].

2.2 Neutron flux

The neutron flux is monitored in beam with a fission chamber [Wen93]. This detector operates on the principle that incident neutrons will occasionally interact with thin ($\approx 400\mu$g/cm^2) backed-foils of fissile material, and that at least one of the two emitted fission fragments will escape the foil to be detected in the ionization chamber.

The number of fissions observed at energy E_n is given by

$$N_f(E_n) = \Phi(E_n) \times \varepsilon_{det} \times \rho_f \sum_i \rho_i \sigma_{f_i}(E_n) \tag{9}$$

where ε_{det} is the efficiency for detecting at least one fission fragment, and ρ_f is the areal number density of fissile nuclei in the fission deposit. The sum in Eq. 9 is over the different fissile materials present in the foil, where the ρ_i are relative atomic fractions.

The areal number density of each fissile material, $\rho_f\rho_i$, is measured by counting α decays from the major constituent of the foil. The current values of $\rho_f\rho_i$ for the major constituents of the fission foils, ^{235}U and ^{238}U, are $1.037(7) \times 10^{18}$ ^{235}U atoms/cm^2 for the ^{235}U foil and $1.05(5) \times 10^{18}$ ^{238}U atoms/cm^2 for the ^{238}U foil [Nel99]. The isotopics, or ρ_i values, provided

by Isotope Product Laboratories are then used to determine ρ_f. The ρ_i values are listed in Table 1.

Table 1: Isotopics in units of atomic fraction, *i.e.* the ρ_i values, for the ^{235}U and ^{238}U fission foils as provided by Isotope Product Laboratories, where the deposit was done. The adopted values of ρ_f are also included in the table.

Nucleus	ρ_i in ^{235}U	ρ_i in ^{238}U
^{234}U	0.0026	7.1×10^{-6}
^{235}U	0.98208	0.00201
^{236}U	0.00937	0.0
^{238}U	0.00595	0.99798
ρ_f	$1.056(7) \times 10^{18}$ atoms/cm^2	$1.05(5) \times 10^{18}$ atoms/cm^2

   The timing resolution of the fission chamber (roughly Gaussian) has a FWHM of about 2 ns, which is much shorter than the HPGe detector timing (≈ 17 ns) used to determine bin widths. In this Section, the neutron energy bin width is assumed to be much larger than the timing uncertainty in the γ-ray counters and neutron flux monitor. In this limit, $\Phi(E_n)$ is the proper quantity to normalize the observed γ-ray counts in an incident neutron energy bin. A more complete discussion of how to normalize and propagate uncertainties, accounting for finite timing resolution, can be found in [You98]. In practice, corrections for finite timing resolution are on order of a few percent.
   For a typical time bin width, the statistical uncertainty in $N_f(E_n)$ is $< 2\%$ for the plutonium experiment. There is possibly some systematic uncertainty in determining N_f which is discussed below. The uncertainty in $\sigma_f(E_n)$ is typically on order of $1-4\%$ for ^{235,238}U which are the fissile materials used in these experiments. Other sources of uncertainty in $\Phi(E_n)$ are from measuring ρ_f and from systematic problems in determining N_f.
   There are two effects which impact the determination of N_f: (1) sometimes neither fission fragment escapes the fission foil and (2) a large background of knockout protons. Carlson [Car74] has derived equations for the fraction of such events as a function of incident neutron energy. Using Equation B of Table 2 from [Car74], the losses have been estimated as a function of incident neutron energy and are shown in Figure 2. For the energy range of interest
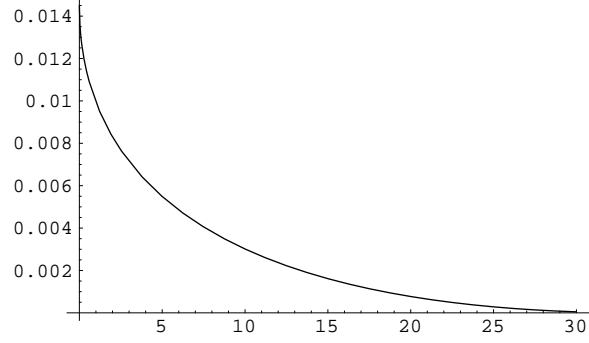
Figure 2: Fission fragment losses in foil (y-axis) as a function of incident energy in MeV (x-axis). Taken from Carlson [Car74], without accounting for center-of-mass angular anisotropy of the fragments which reduces losses in this case.
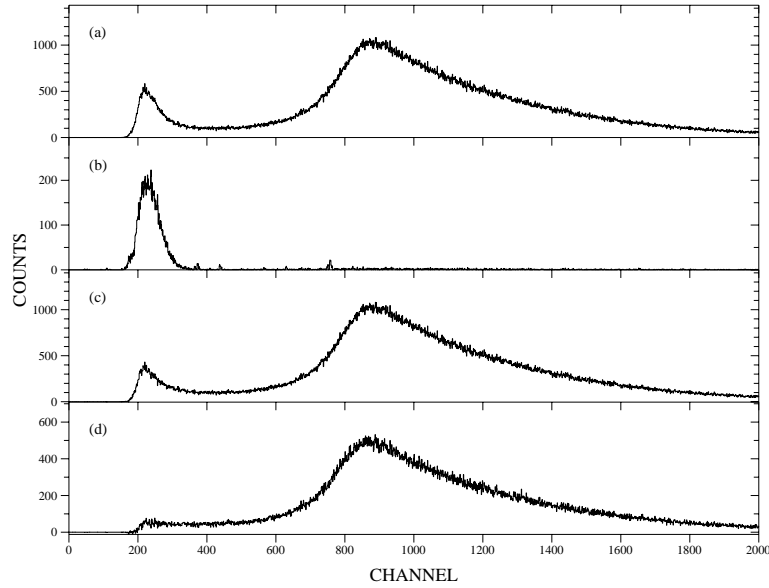
Figure 3: (a) In-beam fission chamber spectrum summed over all neutron energies. (b) Out-of-beam fission chamber spectrum of random alpha-decay events. (c) The difference spectrum (a)-(b). (d) The random-subtracted fission chamber spectrum for $E_n < 11$ MeV.

in the $(n, 2n)$ experiment, losses are $< 0.5\%$, and will be ignored in this analysis. A large background of α decays and proton knockout events are also detected in the ionization chamber. The effects of these events can be seen in Figure 3.

Figure 3a shows the energy spectrum observed in the fission chamber summed over all incident neutron energies. The low-energy peak is from alphas and protons, and the high-energy peak is from the fission fragments. The tail of the fission fragment peak, clearly extends below the low-energy peak. These events need to be counted to arrive at an accurate value of N_f. The out-of-beam spectrum, shown in Figure 3b, contains only counts due to the alpha decay radiation, which are random in time. Figure 3c shows the in-beam spectrum of Figure 3a after the random alpha events are subtracted. It is clear from the figure that there are beam-induced, low-energy events. The time-of-flight spectrum for this low-energy peak, indicates that these events are associated with $E_n \gtrsim 11$ MeV. This suggests that the events are protons, or perhaps alphas. In Figure 3d, the random-subtracted fission chamber spectrum for $E_n < 11$ MeV is shown.

If the low-energy tail of the fission fragment spectrum of Figure 3d is extended in a linear fashion, a simple estimate of the lost counts can be made. About 5.9% of the counts in the fission fragment peak below channel 400. This fraction of lost counts is not a function of neutron energy. Channel 400 was chosen since it is the natural dividing point between the low-energy peak and the fission fragment peak. The uncertainty in the choice of dividing point is within 25 channels of channel 400, indicating an uncertainty of 6.25%. These lost fission events have been folded into ε_{det}, so that $\varepsilon_{det} = 1 - 0.059(4) = 0.941(4)$.

In summary, the number of neutrons in an energy bin, Φ, is given by

$$\Phi(^{235}U) = \frac{1}{\varepsilon_{det}\rho_f} \frac{N_f}{\sum_i \rho_i \sigma_{f_i}} = 1.006(8) \times 10^6 \frac{N_f}{\sum_i \rho_i \sigma_{f_i}} = \frac{N_f}{\varepsilon_n} \tag{10}$$

$$\Phi(^{238}U) = \frac{1}{\varepsilon_{det}\rho_f} \frac{N_f}{\sum_i \rho_i \sigma_{f_i}} = 1.01(5) \times 10^6 \frac{N_f}{\sum_i \rho_i \sigma_{f_i}} = \frac{N_f}{\varepsilon_n} \tag{11}$$

where σ_f is in barns. The uncertainties quoted in Equations 10 and 11 include the statistical uncertainty in determining ρ_f and the systematic uncertainty in determining N_f. Additional uncertainty in σ_f (1-4%) and in N_f statistics ($< 2\%$) are included in the work done by [Ber00] and [You00]. As discussed above, N_f is the number of counts above threshold minus the number of random pulse heights. The functional dependence of ε_n is shown in Figure 4 for the ^{235}U fission foil for the neutron energy range of interest in the $(n, 2n)$ measurements. The neutron flux is computed for the weighted centroid of each bin, determined as discussed in [You98].
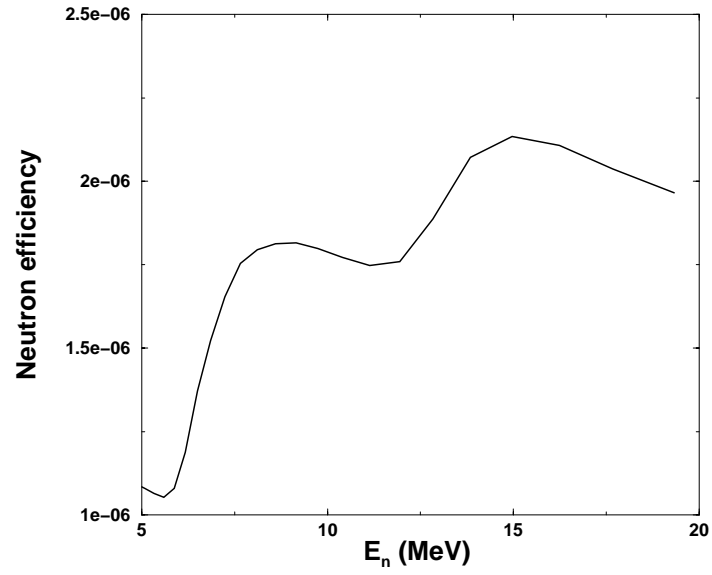
Figure 4: Efficiency for detecting neutrons, ε_n, with the ^{235}U fission chamber.

3 Target areal density

In this section we are interested in the areal density, ρl, and its uncertainty for the targets used for in-beam experiments. Where possible, three independent approaches to determining ρl are discussed: (1) assume ρ based on previous measurements and measure thickness, and (2) assume l and ρ do not vary across surface and calculate M/A, where M is mass of target and A is its surface area, and (3) assume attenuation coefficient, μ, and measure the attenuation of 165.9 keV photons ([139]Ce source) through target. Only the third method accounts for variations in both density and thickness across the target. However, the first method accounts for the more likely variations in target thickness.

The photon attenuation measurements were made with a [139]Ce source. A 2-inch thick lead brick collimator with a 5/8-inch diameter hole was placed six inches from the [139]Ce source. The target was located six inches from the lead source collimator. An identical lead brick, used to collimate a Ge detector, was placed an additional six inches further from the source. The Ge detector was used to observe the unattenuated source photons from behind the second lead brick. All told, 12 inches separate the inner faces of the two lead collimators, with the target in the middle. This geometry effectively samples a 1/2-inch diameter spot on the target. In addition, a [133]Ba source was placed behind the second brick in order to serve as a clock monitor for the experiment.

Note that the appropriate value of density, ρ, to be used in Eq. 8 accounts only for the isotopic content of the target nuclei relevant to the measurement, $e.g.$ [239]Pu content of the Pu target. The effect of the non-[239]Pu content of the target must be accounted for. The gallium content of the Pu foil can be neglected for the source attenuation measurements.

3.1 LANL plutonium targets

3.1.1 Density-thickness approach

The foils were made with delta-phase plutonium which has an evaluated density of 15.9(1) g/cm^3 at 319°C [Sub]. These foils are gallium-stabilized at room temperature by including 0.987(2)% gallium by weight [Nel99]. The density of gallium is 5.904 g/cm^3. The density for this mixture of gallium and plutonium is 15.75(5) g/cm^3 [Gal99].

Table 2 lists the isotopic content of the plutonium targets given by different measurements at LANL and AWE. The two LANL measurements were done by mass spectroscopy. There were three AWE measurements, but the method used is not known. In Table 2 the average values and the uncertainties are taken from the standard deviation of the measurements. There is an $\approx$ 0.4% discrepancy between the LANL and AWE measurements in the amount of [239,240]Pu. There are two possible reasons for this discrepancy: (1) a molten salt reduction process undertaken by Jason Lashly and Mike Blau in order to reduce [241]Am content was done after the AWE measurement and (2) the AWE analysis was done on a different batch of material. Hence, the average of the LANL values, 98.0138(11)% (or 98.0053(11)% by weight) has been adopted. Including the gallium and other isotopes of plutonium, the [239]Pu content is 97.038(2)% by weight. From Table 2, the [238]Pu content is very small. Even if the [238]Pu(n, n') cross section was as high as 10 barns, the contamination in measured γ-ray yields would be negligible. On the

other hand, contamination from ^{240}Pu$(n, 3n)$ will be at the 1-5% for incident neutron energies above 18 MeV.

Table 3 lists the thickness and diameter measurements of the 10-mil and 20-mil foils. The thickness was measured in ten different spots on each plutonium foil. Measurements 1 through 8 were taken around the edge of the disk equally spaced, and measurements 9 and 10 were taken just off center of each disk. The adopted thickness values were derived by taking a weighted average of the ten data points, where measurements 9 and 10 were weighted by a factor of four each because the neutron flux is peaked at the center of the target. Hence, $0.01083 \pm .00026$ inch is adopted for the thickness of the 10-mil foil and 0.01971 ± 0.00009 inch is adopted for the thickness of the 20-mil foil. In both cases the uncertainty in this approach was determined from the dispersion in the values from Table 3 which were used to determine the weighted average.

Hence, the ρl values in this approach is given in this way: (1) $\rho = 15.75(5)$ g/cm^3 and (2) l is $0.02751(66)$ cm and $0.05006(23)$ cm for 10-mil and 20-mil foils, respectively. This implies that $\rho l = 0.4333(105)$ g/cm^2 for the 10-mil foil and $\rho l = 0.7884(56)$ g/cm^2 for the 20-mil foil. The areal density of ^{239}Pu is given by folding in the mass fraction $= 0.97038(2)$, which implies that the effective $\rho l = 0.4205(102)$ g/cm^2 for the 10-mil foil and $\rho l = 0.7650(54)$ g/cm^2 for the 20-mil foil.

3.1.2 Mass-area approach

The masses of the foils were measured on a scale: the 10-mil is 3.4(1) grams the 20-mil foil is 6.4(1) grams. Clearly, the mass measurements are a limitation on the accuracy of this approach.

The foil diameter was measured three times (measurements 11 through 13 in Table 3) on the 10-mil foil, but not on the 20-mil foil. These three measurements were taken equally spaced on the diameter of the 10-mil disk. The same die was used to cut both foils, and the requested tolerance on the die is 1.255 ± 0.002 inch. Since the diameter measurements on the 10-mil foil are within that tolerance, a diameter value of 1.255 ± 0.002 inch is assumed for both foils.

Hence, the ρl values in this approach is given in this way: (1) masses are 3.4(1) g and 6.4(1) g for 10-mil and 20-mil foils, respectively, and (2) the area $A = 7.981(25)$ cm^2 for both foils. This implies that $\rho l = 0.4260(132)$ g/cm^2 for the 10-mil foil and $\rho l = 0.8019(132)$ g/cm^2 for the 20-mil foil. After folding in the mass fraction $= 0.97038(2)$ as given above, the effective ρl values are $\rho l = 0.4134(128)$ g/cm^2 for the 10-mil foil and $\rho l = 0.7781(128)$ g/cm^2 for the 20-mil foil.

3.1.3 Photon attenuation approach

The attenuation measurements gave $\rho l = 0.4305(109)$ g/cm^2 for the 10-mil foil and $\rho l = 0.8510(207)$ g/cm^2 for the 20-mil foil. After folding in the mass fraction $= 0.97038(2)$ as given above, the effective ρl values are $\rho l = 0.4177(106)$ g/cm^2 for the 10-mil foil and $\rho l = 0.8258(201)$ g/cm^2 for the 20-mil foil.

3.1.4 Summary

See Table 9 for a summary of adopted target areal densities.

Table 2: Isotopics of Pu targets as measured by LANL and AWE. Values are given in percents by weight. The LANL assays are referenced by ROD12016RN. The AWE values are referenced by CBD005300, CBD005200, and CBD004200. The LANL ^{241}Am measurement was done separately via chemical separation.

Nuclide	ROD12016RN #1	ROD12016RN #2	LANL average
^{238}Pu	0.0036	0.0018	0.0027(13)
^{239}Pu	98.0130	98.0145	98.0138(11)
^{240}Pu	1.9750	1.9716	1.9733(24)
^{241}Pu	0.0074	0.0112	0.0093(27)
^{242}Pu	0.0016	0.0009	0.0013(5)
^{241}Am			< 0.0002

Nuclide	CBD005300	CBD005200	CBD004200	AWE
^{238}Pu	0.0	0.0	0.0	0.0
^{239}Pu	98.335	98.592	98.449	98.41(14)
^{240}Pu	1.656	1.401	1.544	1.52(13)
^{241}Pu	0.0079	0.0063	0.0066	0.0069(9)
^{242}Pu	0.0011	0.0063	0.0095	0.006(5)
^{241}Am	0.0548	0.0489	0.0533	0.052(3)

Table 3: Thickness and diameter measurements of the 10-mil and 20-mil plutonium foils. The locations of these measurements are discussed in the text.

Measurement	10-mil (in)	20-mil (in)
1	0.0111	0.0196
2	0.0100	0.0196
3	0.0105	0.0197
4	0.0109	0.0198
5	0.0111	0.0199
6	0.0109	0.0198
7	0.0106	0.0197
8	0.0109	0.0196
9	0.0109	0.0197
10	0.0109	0.0197
11	1.256	
12	1.254	
13	1.255	

Both approaches to determining ρl are mostly independent of each other and yield mostly consistent results. The only significant discrepancy is that the ρl value obtained from the photon attenuation measurement is about 2.3σ from the mean of the other two methods. It is possible that there are significant variations in the areal density across the 20-mil target, but the large uncertainty ($\approx 2.4\%$) in the photon attenuation method is not strong enough to make this claim. Therefore, the adopted values are obtained by averaging the results of each approach, properly weighted by the uncertainty. However, the quoted uncertainties reflect differing assumptions about variations in thickness and density. The adopted ρl values are $0.4305(66)$ g/cm^2 for the 10-mil foil and $0.7939(50)$ g/cm^2 for the 20-mil foil. The adopted effective (folding in the mass fraction of ^{239}Pu) ρl values are $0.4177(64)$ g/cm^2 for the 10-mil foil and $0.7704(48)$ g/cm^2 for the 20-mil foil.

3.2   Uranium-235 targets used in 1998

The uranium targets consist of 2-4 laminated packets of uranium foils. Each packet contains 2 foils, which were rolled and cut separately. The "12-mil" target consisted of two packets, or four foils, whereas the "24-mil" target consisted of four packets, or eight foils. Each foil is approximately 3 mils in thickness.

3.2.1 Density-thickness approach

The thicknesses of the uranium foils have not been measured so this approach is not viable. Not only are the plastic laminate covers stuck to the uranium foils, but also the surfaces often appear to be highly irregular and wrinkled. A thickness of 3(1) mils or 0.00769(25) cm for each foil, which is the nominal value with a large uncertainty, is adopted in order to proceed with the analysis as a check. This would imply that the 12-mil target has a thickness of 0.0308(50) cm and the 24-mil target has a thickness of 0.0615(71) cm.

The density of natural uranium has an accepted value of 18.95(3) g/cm^3. However, natural uranium contains only small amounts of ^{235}U. The density of pure ^{235}U would be about 18.71(3) g/cm^3. There is no specific information on whether any other elements are present in the foils. The foils are 93.15% ^{235}U by molar fraction. Assuming that the remainder of the target is ^{238}U, then the mass fraction is 93.08(2)%, and the density is about 18.73(3) g/cm^3.

Hence, the ρl values in this approach are given in this way: (1) mass fraction = 0.9308(2), (2) ρ = 18.73(3) g/cm^3, and (3) l is 0.0308(50) cm and 0.0615(71) cm for 12-mil and 24-mil foils, respectively. The ρl values are ρl = 0.58(10) g/cm^2 for the 12-mil foil and ρl = 1.15(13) g/cm^2 for the 24-mil foil. This implies that the effective ρl = 0.54(9) g/cm^2 for the 12-mil foil and ρl = 1.07(12) g/cm^2 for the 24-mil foil.

3.2.2 Mass-area approach

The mass of each foil packet was measured on a scale. The mass of the laminate was estimated by weighing a separate piece of laminate which was the same size used for the foil packets. The adopted weight of the plastic laminate is 0.35(2) g. Table 4 lists the masses of each foil packet after adjusting for the plastic laminate, as well as the dimensions of each foil.

The 12-mil target was comprised of Packet 1 and Packet 2 stacked together. The 24-mil target was comprised of all four packets stacked together. Assuming the uncertainties quoted in Table 4 can be combined in a statistical fashion, then the ρl values in this approach are given in this way: (1) mass fraction = 0.9308(2) as given above, and (2) the M/A values derived from Table 4 are 0.563(10) gm/cm^2 and 1.077(11) gm/cm^2 for the 12-mil and 24-mil targets, respectively. This implies that ρl = 0.524(9) g/cm^2 for the 12-mil foil and ρl = 1.002(10) g/cm^2 for the 24-mil foil.

3.2.3 Photon attenuation approach

The attenuation measurements gave ρl = 0.5012(135) g/cm^2 for the 12-mil target and ρl = 0.9960(193) g/cm^2 for the 24-mil target. After folding in the mass fraction = 0.9308(2) as given above, the effective ρl values are ρl = 0.4665(126) g/cm^2 for the 12-mil target and ρl = 0.9271(180) g/cm^2 for the 24-mil target. The attenuation of the plastic laminate can be ignored.

Table 4: Mass, length, and width measurements of the uranium foils. The uncertainties in mass are uncertainties in the measurement. The uncertainties in length and width are from the standard deviation of several measurements along each side. The uncertainty in the packet area is from averaging the foil areas plus 50% of the difference in the foil areas, since the weighting between the two foils is unknown.

Foil	Mass (g)	Length (cm)	Width (cm)	Area (cm^2)	ρl
Foil 1	-	3.87(8)	4.02(2)	15.56(33)	-
Foil 2	-	3.91(3)	4.08(8)	15.95(34)	-
Packet 1	4.20(2)	-	-	15.76(45)	0.266(8)
Foil 3	-	3.84(7)	4.04(4)	15.51(32)	-
Foil 4	-	3.84(7)	4.04(4)	15.51(32)	-
Packet 2	4.60(2)	-	-	15.51(32)	0.297(6)
Foil 5	-	3.93(3)	3.83(2)	15.05(14)	-
Foil 6	-	3.99(2)	3.80(1)	15.18(9)	-
Packet 3	3.94(2)	-	-	15.12(19)	0.261(4)
Foil 7	-	3.85(3)	3.88(1)	14.95(12)	-
Foil 8	-	3.83(1)	3.86(1)	14.78(5)	-
Packet 4	3.76(2)	-	-	14.87(22)	0.253(4)

3.2.4   Summary

The results of the mass-area and the photon attenuation approaches to determining ρl are not consistent with each other, and the uncertainty in the density-thickness approach is so large that the comparison with this result is not very helpful. Because these targets are visibly wrinkled, one would have a tendency to favor the photon attenuation measurements since thickness variations are folded directly into the measurement. However, it is not clear that spot averaged over in the photon attenuation measurement is the same as the spot that was in beam. If we assume that the thickness variations affect our measurement at a 10% level for each foil, then this will result in an additional 5% uncertainty in the 12-mil target ρl and an additional 3.5% uncertainty in the 24-mil target ρl.

Hence, unless repeat measurements can help to resolve the discrepancy, at this time we can only be confident in ρl to about 7% for the 12-mil target and about 5% for the 24-mil target.

3.3   Uranium-235 targets used in 1999

Because of the poor quality and imprecise measurements of the ^{235}U foils used in 1998, seven new foils were obtained in October 1999. These foils were well-characterized before being laminated. The foils were labeled #1-#7 by Ron Nelson, and labeled E267-E273 by Bremser

and Gross [Bre99], who characterized the foils. The uranium target used for the experiment in November 1999 consisted of 2 laminated packets of uranium foils. One packet contained foils #2 and #3, and the other packet contained foils #4 and #5. Foils #6 and #7 were also laminated in one packet and foil #1 was laminated separately, but these two laminated packets were not used. Each packet contains two, approximately 3-mil foils, which were rolled and cut separately.

3.3.1 Density-thickness approach

The foil densities were determined via immersion using ethylene glycol as the suspension fluid [Bre99]. Table 6 summarizes these measurements. Based on the standard deviation of the measurements, the precision of this technique is about 1.6%. Thickness measurements were made with a Sarrett Digital Micrometer #734MXFL, which has an accuracy of 0.0003 cm. The thickness measurements are summarized in Table 5. The thicknesses of the seven ^{235}U foils were measured in 9 different spots defined by a 3X3 lattice of points [Bre99]. The adopted thickness for each foil is the average of the nine measurements, and the adopted uncertainties include the stated 0.0003 cm accuracy and the standard deviation of the measurements added in quadrature.

In this approach, the ρl value of the target is given by the sum of the ρl values for foils #2-#5, or 0.552(24) g/cm^2. The uncertainty was derived by adding all uncertainties in quadrature, except the 4.0% uncertainty in the accuracy of the thickness measurements, which was added in quadrature separately. The ^{235}U mass fraction value for these foils is 0.9323. This gives an effective areal density of ^{235}U of 0.515(22) g/cm^2.

3.3.2 Mass-area approach

The mass of each foil was measured using a Mettler AE200 electronic balance, which has an accuracy of 0.0003 g. The foils are square and their length and widths were measured several times along each side with a Mitutuyo Absolute Digimatic Caliper with an accuracy of 0.002 cm. The mass, length, and width measurements are summarized in Table 7. As explained above, the target consisted of Foils #2-#5. Hence, the ρl value derived from this approach is 0.4828(27) g/cm^2. The ^{235}U mass fraction value is 0.9323. This gives an effective areal density of ^{235}U of 0.4501(25) g/cm^2.

Table 6: The density of the seven ^{235}U foils was measured via immersion using ethylene glycol as the suspension fluid [Bre99]. This approach was used nine times for each foil and the results are summarized here. These foils are labeled as E2##-# for reference purposes.

	E267-1	E268-2	E269-3	E270-4	E271-5	E272-6	E273-7
Meas. #1	17.9858	18.4444	18.7985	18.6297	18.3378	18.6821	18.9621
Meas. #2	18.4050	18.5736	18.5971	18.5925	18.2642	18.2572	18.6991
Meas. #3	18.8841	18.5279	18.3999	18.0547	18.6875	19.0906	18.9191
Meas. #4	18.2171	18.4493	18.5995	18.7568	18.2265	18.2595	18.4791
Meas. #5	18.9669	18.9518	18.2069	18.1342	18.5328	18.6053	18.2617
Meas. #6	18.6661	18.1366	18.0227	18.4061	18.3021	17.9976	18.1428
Meas. #7	18.7522	18.0882	18.2386	19.1165	18.4506	18.3617	18.3017
Meas. #8	18.3597	18.6048	18.7574	18.6695	18.6087	18.4033	18.6442
Meas. #9	18.1905	18.0495	18.0443	18.5877	18.4916	18.6821	18.6079
Average	18.49	18.43	18.41	18.55	18.43	18.48	18.56
Std. Dev.	0.34	0.29	0.30	0.32	0.16	0.32	0.29

Table 7: Mass, length, and width measurements of the ^{235}U foils. The uncertainties include the accuracy of the measurements as discussed in the text. The uncertainties in length and width also include the standard deviation of several measurements along each side.

Foil	Mass (g)	Length (cm)	Width (cm)	Area (cm^2)	ρl
Foil 1	0.7117(3)	2.571(16)	2.567(23)	6.600(73)	0.1078(11)
Foil 2	0.7607(3)	2.568(07)	2.557(34)	6.566(85)	0.1159(13)
Foil 3	0.7739(3)	2.563(39)	2.503(02)	6.414(96)	0.1207(15)
Foil 4	0.7884(3)	2.490(06)	2.555(34)	6.361(89)	0.1239(14)
Foil 5	0.7957(3)	2.572(12)	2.529(26)	6.505(72)	0.1223(11)
Foil 6	0.7920(3)	2.548(25)	2.523(23)	6.429(84)	0.1232(13)
Foil 7	0.7086(3)	2.546(10)	2.545(06)	6.481(32)	0.1093(05)

Table 5: The thicknesses of the seven ^{235}U foils were measured in 9 different spots defined by a 3X3 lattice of points [Bre99]. The results are listed here, as well the standard deviation of the nine measurements for each foil. This standard deviation is added in quadrature with the accuracy of 0.0003 cm to arrive at the adopted average values and uncertainties.

	E267-1	E268-2	E269-3	E270-4	E271-5	E272-6	E273-7
Meas. #1	0.0075	0.0074	0.0077	0.0080	0.0079	0.0074	0.0061
Meas. #2	0.0075	0.0072	0.0075	0.0077	0.0076	0.0074	0.0065
Meas. #3	0.0070	0.0072	0.0076	0.0074	0.0076	0.0071	0.0066
Meas. #4	0.0074	0.0072	0.0076	0.0075	0.0077	0.0071	0.0056
Meas. #5	0.0075	0.0067	0.0072	0.0075	0.0079	0.0071	0.0064
Meas. #6	0.0072	0.0072	0.0075	0.0075	0.0072	0.0070	0.0056
Meas. #7	0.0074	0.0071	0.0075	0.0075	0.0075	0.0070	0.0050
Meas. #8	0.0071	0.0071	0.0072	0.0076	0.0076	0.0070	0.0060
Meas. #9	0.0069	0.0074	0.0071	0.0077	0.0076	0.0069	0.0060
Std. Dev.	0.0002	0.0002	0.0002	0.0002	0.0002	0.0002	0.0005
Adopted	0.0073(4)	0.0072(4)	0.0075(4)	0.0076(4)	0.0076(4)	0.0071(4)	0.0060(6)

3.3.3 Photon attenuation approach

The attenuation measurements gave $\rho l = 0.4828(136)$ g/cm^2 for the 12-mil target. After folding in the mass fraction $= 0.9323$, the effective ρl value is $\rho l = 0.4501(126)$ g/cm^2.

3.3.4 Summary

See Table 9 for a summary of adopted target areal densities.

The areal density of $0.514(22)$ g/cm^2 obtained via that density-thickness approach is inconsistent with the values obtained from the other two approaches ($0.4828(27)$ and $0.4828(136)$ g/cm^2). Hence, the density-thickness approach is suspect. The density is unlikely to be wrong since it is within a few percent of the canonical value. This would suggest that the thickness measurements are wrong. Given the difficulty of measuring these thicknesses with a micrometer, we have discarded the density-thickness approach and adopted the weighted average of the other two measurements. This yields an areal density of $0.4828(27)$ g/cm^2. After folding in the mass fraction $= 0.9323$, the effective ρl value is $\rho l = 0.4501(25)$ g/cm^2.

3.4 Natural iron targets

The iron target for iron-only measurement consisted of 2 natural iron foils, each with a nominal thickness of 20 mils. The foils were acquired from Goodfellow.

3.4.1 Density-thickness approach

The thicknesses of these foils have not been measured.

The density of natural iron has an accepted value of 7.874 g/cm^3. According to the Goodfellow catalogue, these foils typically are 99.5% natural iron. The accepted mass fraction of ^{56}Fe in natural iron is $0.918(1)$.

3.4.2 Mass-area approach

The two foils have masses of $10.07(2)$ and $10.09(2)$ grams. Each foil is square with length $5.0406(52)$ cm. This implies an area of $25.408(37)$ cm^2, and hence M/A values of $0.3963(6)$ gm/cm^2 and $0.3971(6)$ gm/cm^2, respectively.

The target was comprised of both foils stacked together. The ρl values in this approach are given in this way: (1) mass fraction is assumed to be $0.995 \times 0.918(1) = 0.913(2)$, and (2) the M/A value derived above is $0.7934(8)$ gm/cm^2. This implies that $\rho l = 0.7244(16)$ g/cm^2.

3.4.3 Summary

See Table 9 for a summary of adopted target areal densities.

The mass-area approach is very precise and gives a $rhol$ of $0.7244(16)$ g/cm^2.

3.5   Natural iron monitor foils

The iron monitor foils usually consisted of four natural iron foils, each with a nominal thickness of 2 mils. Normally, two of the foils were placed on the upstream side of target and two of foils were placed on the downstream side. Ten foils were acquired from Goodfellow. Four of the foils were circular and the other six were square.

The mass, diameter, and thickness measurements of these foils are listed in Table 8. The scale used to do the mass measurements tested linearly in the range of interest and had an uncertainty of about 0.0005 grams. The uncertainty in the diameter measurements is estimated at about 0.002 due the inherent difficulties in measuring a foil which bends. The uncertainty in the thickness measurements due to limitations in the micrometer is about 0.0002 inches, or about 9%.

The density of natural iron has an accepted value of 7.874 g/cm^3. According to the Goodfellow catalogue, typical purities are better than 99.5%. The accepted mass fraction of ^{56}Fe in natural iron is 0.918(1).

3.5.1   Summary

Despite the large uncertainty in the thickness measurements, the M/A approach supports the notion that the foils are somewhat thicker than the nominal value quoted by Goodfellow. The M/A values for the areal density, or *Areal density #1* values are recommended for these foils.

Table 8: Mass, area, and thickness measurements of the ^{nat}Fe foils used as a monitor of the neutron flux in beam.

Measurement	Foil #5	Foil #7	Foil #8	Foil #10
Weight (g)	0.6346(5)	0.6540(5)	0.6315(5)	0.6286(5)
Diameter (in)	1.754	1.749	1.754	1.758
	1.752	1.751	1.749	1.754
	1.753	1.749	1.755	1.756
Average	1.753(2)	1.750(2)	1.753(2)	1.756(2)
Area (cm^2)	15.57(16)	15.51(16)	15.57(16)	15.62(16)
Areal density #1 (g/cm^2)	0.0408(4)	0.0422(4)	0.0406(4)	0.0402(4)
Thickness (in)	0.0022	0.0021	0.0021	0.0020
	0.0020	0.0023	0.0021	0.0021
	0.0021	0.0023	0.0022	0.0021
	0.0022	0.0025	0.0022	0.0023
	0.0021	0.0024	0.0021	0.0021
Average	0.0021(2)	0.0023(2)	0.0021(2)	0.0021(2)
Areal density #2 (g/cm^2)	0.0424(38)	0.0464(42)	0.0428(39)	0.0424(38)

Measurement	Foil #1	Foil #2	Foil #3	Foil #4	Foil #6	Foil #9
Weight (g)	1.0429	1.0345	0.9900	1.0293	1.0163	1.0539
Length (in)	1.968	1.947	1.942	1.958	1.983	1.973
	1.972	1.950	1.937	1.957	1.975	1.982
	1.976	1.954	1.926	1.955	1.984	1.977
Average	1.972	1.950	1.935	1.957	1.981	1.977
Width (in)	1.974	1.993	1.994	1.954	1.948	1.954
	1.970	1.988	1.988	1.958	1.942	1.961
	1.976	1.987	1.976	1.965	1.953	1.963
Average	1.973	1.989	1.986	1.959	1.948	1.959
Area (cm^2)	25.1058	25.0313	24.7929	24.7297	24.8882	24.9951
Areal density #1 (g/cm^2)	0.0415	0.0413	0.0399	0.0416	0.0408	0.0422

3.6 Overall summary

Table 9: Summary of the "effective" target ρl values determined via three approaches after correcting for mass fraction: (1) density-thickness, (2) mass-area, and (3) photon attenuation. The final adopted values are also included and are discussed in the text summaries for each target.

Target	ρl #1 (g/cm^2)	ρl #2 (g/cm^2)	ρl #3 (g/cm^2)	Adopted ρl (g/cm^2)
^{239}Pu 10-mil	0.4205(102)	0.4134(128)	0.4177(106)	0.4177(64)
^{239}Pu 20-mil	0.7650(54)	0.7781(128)	0.8258(201)	0.7704(48)
^{235}U 12-mil (1998)	0.54(9)	0.524(9)	0.4665(126)	-
^{235}U 24-mil (1998)	1.07(12)	1.002(11)	0.9271(180)	-
^{235}U 12-mil (1999)	0.515(22)	0.4501(25)	0.4501(126)	0.4501(25)
^{56}Fe 40-mil		0.7244(16)		0.7244(16)

4 Absolute peak efficiency for a point source

The next three sections concern determining the absolute peak efficiency for the array as a function of photon energy. The absolute peak efficiency of a detector is defined as the probability that the full energy of the photon is deposited in an active area of the detector crystal. While it is straightforward to measure the absolute peak efficiency of an array for a low count-rate point source, it is more complex to do so for an extended source when deadtime effects are appreciable. The approach for this experiment is to (1) measure the array efficiency with a known point source (Section 4), (2) correct for geometrical effects which lower the efficiency to detect γ rays from the edges of an extended source (Section 5), and (3) correct for γ-ray attenuation in the target (Section 6).

The point source efficiency measurements are discussed in Section 4.1. The NIST-traceable source strengths provided by the vendor were independently measured at LLNL and found to agree. To be consistent with others in the group the sorting routines used to sort the efficiency data were based on the routines developed by Walid Younes [You98b] to sort the in-beam data. The measurements are in good agreement with expectations based on MCNP calculations and with numbers provided by Ortec.

Measuring the point source efficiency requires an accurate determination of deadtime, or the probability that a pulse height in a detector is *not* histogrammed offline. The experimental method of measuring the deadtime correction is outlined in Section 4.2. This procedure is validated by comparing the measured deadtime to independently estimated deadtimes. Tests of the deadtime correction procedure were performed at a variety of array rates to investigate rate-dependent effects.

The work presented here has been largely automated by developing various codes and scripts. An overview of the codes and scripts used, and their locations on dollar.llnl.gov can be found in Appendix A.

4.1 Point source measurements

4.1.1 Source strength

Several calibrated, NIST-traceable, mixed γ-ray source standards were acquired from Analytics, Inc. of Atlanta, Georgia. Energies, source strengths, and source lifetimes of source 56343-28 — the point source used to make the measurements described in this section — are tabulated in Table 10. One unexpected property of the mixed γ-ray source was the presence of very strong cesium x rays which resulted in larger detector rates (≈ 400 Hz) than anticipated.

After using the source to make several measurements, the source was measured by Cindy Conrado at the detector laboratory in LLNL's Isotopes Science Division [Con99]. This measurement occurred about 8 months after acquiring the source, so the 279-keV line in ^{203}Hg had decayed significantly. The results of this measurement are also listed in Table 10 for comparison. It should be noted that the LLNL measurement made no attempt to correct for systematic uncertainties. In addition, the LLNL detector system has not been calibrated in over 20 years. In this light, the agreement between both measurements is remarkably good. The Analytics numbers have been adopted throughout the analysis.

Table 10: Relevant details on the calibrated, NIST-traceable, mixed γ-ray source used for the point source efficiency measurement. The calibration was performed on July 1, 1998 12:00 EST. The half-lives were obtained from Richard Helmer [Hel98] The LLNL measured values are listed for comparison. The Analytics uncertainties include systematic effects, whereas the LLNL uncertainties are purely statistical.

γ-ray (keV)	Isotope	Half-life	Analytics		LLNL	
			γ/sec	Uncertainty (%)	γ/sec	Uncertainty (%)
60	^{241}Am	157850(240) d	3285	1.4	3458	1.1
88	^{109}Cd	461.4(12) d	4748	1.4	4817	1.1
122	^{57}Co	271.79(9) d	2529	1.3	2540	0.8
166	^{139}Ce	137.641(20) d	4102	1.2	4074	0.7
279	^{203}Hg	46.595(13) d	7619	1.4	8053	10.4
392	^{113}Sn	115.09(3) d	4802	1.2	4690	1.2
662	^{137}Cs	10964(9) d	3134	1.3	3074	0.6
898	^{88}Y	106.630(25) d	12530	1.3	12151	1.1
1173	^{60}Co	1925.3(3) d	6082	1.3	5935	0.5
1332	^{60}Co	1925.3(3) d	6121	1.3	5967	0.5
1836	^{88}Y	106.630(25) d	13180	1.3	12845	1.1

4.1.2 Measurement results and uncertainties

Examples of point source spectra for a typical planar and typical coaxial Ge detector are shown in Figures 5 and 6. The most striking difference between the coaxial and planar detector spectra is the roll-off in efficiency at low energies for the coaxial detectors. The coaxial spectrum shows clear evidence of a hardware reduction in efficiency, while the planar spectrum does not. The constant fraction discriminators (CFDs) used for the coaxial detectors are of poorer quality than the ones used for the planar detectors. The CFDs for all detectors are set above the ADC low-energy threshold in order to ensure that the deadtime correction discussed below is not overestimated. If the CFD threshold is below the ADC lower-level discriminator then clean pulses will be counted by the scaler, but will not be converted in the ADC. Raising the coaxial CFDs electronic cutoff resulted in reduced efficiency for energies as high as 500 keV in some coaxial detectors.

The point source efficiency was measured on 10/1/98, 1/5/99, and 6/28/99 by different experimenters. Each time the point source was aligned in the array using a transit. The counting rate, and hence deadtime correction, varied between 25-50%. In principle, these three measurements should agree within statistical uncertainty. However, the agreement is worse than statistical expectation. Of particular note, the three measurements showed substantial disagreement for coaxial detectors below about 350 keV, with a factor of 2 discrepancy at ≈ 100 keV. This is probably due to drift of the coaxial-detector CFD thresholds over time. When excluding energies below 350 keV in the coaxial detectors, a statistical analysis of the distribution of these three measurements indicates that there is an additional uncertainty of $\approx 3\%$ in the efficiency
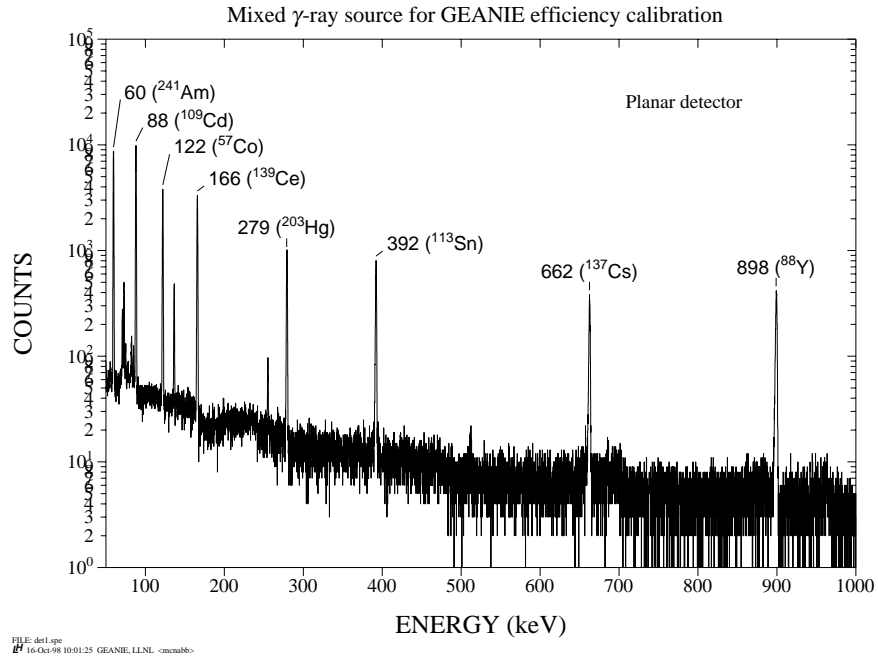
Figure 5: Mixed γ-ray source spectrum for a typical planar detector.
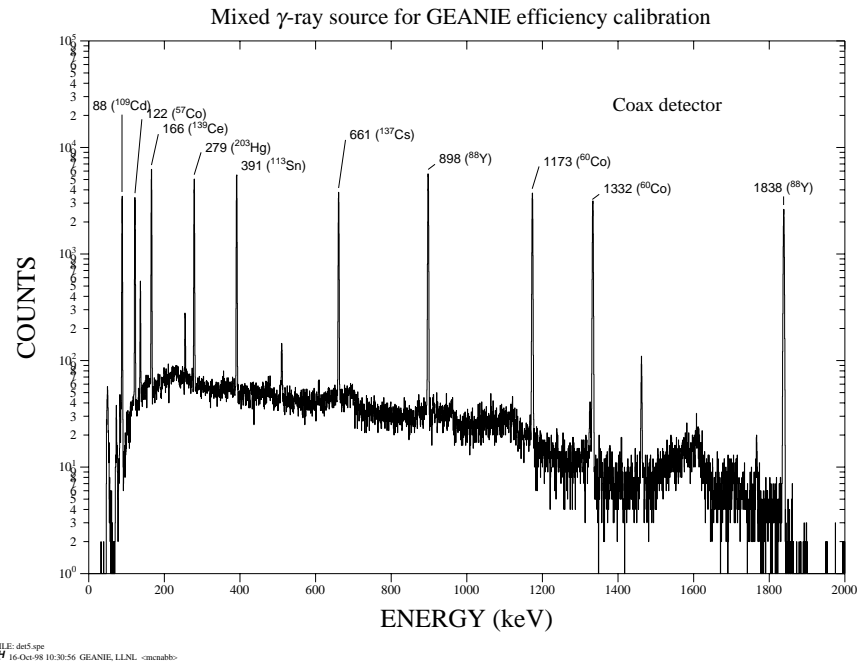
Figure 6: Mixed γ-ray source spectrum for a typical coaxial detector.

of a particular detector at a particular energy. This additional "experimenter" uncertainty is

probably due to variation in the exact placement of the point source with respect to the center of the array, but may possibly be due to other factors.

The point source efficiency is taken to be the statistically-weighted average of these three measurements. The results are tabulated in Table 11. The peak areas were determined by summing and subtracting a background determined by the flat upper limit method [Cro95]. Systematic uncertainties in determining the background counts were included. The efficiency, $\varepsilon(E_\gamma)$, of a detector for a particular γ ray with energy E_γ is given by

$$\varepsilon = \frac{N}{T_{live}S(\Delta T)} \tag{12}$$

where N is the number of observed counts, S is the source strength, and T_{live} is the detector livetime or probability that pulse height is histogrammed offline. The uncertainty in S includes the propagation of uncertainty in the initial calibration as well as the uncertainty in the isotope lifetime. The experiment time ΔT was determined by scaling a clock for which the uncertainty is negligible. The procedure for determining T_{live} is discussed in detail in Section 4.2. The uncertainty in T_{live} is also considered negligible. The uncertainty in source strength should not be added in quadrature when combining all detectors. Therefore this uncertainty, approximately 1.5%, is not propagated through the efficiency analysis, but is accounted for in the final cross section analysis.

Table 11: Point source efficiencies as measured for the mixed γ-ray point source lines. Uncertainties include the uncertainty in peak area determination and the "experimenter" uncertainty discussed in the text. An additional 1.5% uncertainty in source strength should be included after analysis of all detectors. Energies below 350 keV in the coaxial detectors are excluded as explained in the text.

Det.	59.541	88.034	122.06	165.86	279.19	391.70	661.66	898.04	1173.3	1332.5	1836.1
A	0.004321(133)	0.004089(126)	0.003544(109)	0.002611(80)	0.001236(42)	0.000744(23)	0.000364(11)	0.000238(8)	-	-	-
B	0.004141(127)	0.004319(133)	0.003984(123)	0.003044(93)	0.001491(50)	0.000957(30)	0.000487(15)	0.000329(10)	-	-	-
C	0.004219(130)	0.004312(133)	0.003976(122)	0.003013(92)	0.001469(49)	0.000925(29)	0.000461(14)	0.000309(10)	-	-	-
D	0.004174(128)	0.004203(130)	0.003910(120)	0.003037(93)	0.001496(50)	0.000944(29)	0.000480(15)	0.000324(10)	-	-	-
E	-	-	-	-	-	0.001649(81)	0.001108(55)	0.000851(42)	0.000683(34)	0.000612(30)	0.000481(24)
F	-	-	-	-	-	0.001370(68)	0.000870(43)	0.000658(33)	0.000525(26)	0.000471(23)	0.000357(18)
G	-	-	-	-	-	0.001397(69)	0.000875(43)	0.000659(33)	0.000531(26)	0.000472(23)	0.000362(18)
H	-	-	-	-	-	0.001378(68)	0.000839(41)	0.000683(34)	0.000549(27)	0.000488(24)	0.000392(19)
I	0.004165(128)	0.004176(129)	0.003772(116)	0.002863(88)	0.001388(46)	0.000870(27)	0.000434(13)	0.000293(9)	-	-	-
J	0.004192(129)	0.004229(130)	0.003882(120)	0.002952(90)	0.001452(48)	0.000894(28)	0.000445(14)	0.000294(9)	-	-	-
K	0.004028(124)	0.004043(124)	0.003687(114)	0.002813(86)	0.001411(47)	0.000869(27)	0.000439(14)	0.000295(9)	-	-	-
L	0.003176(98)	0.003742(115)	0.003442(106)	0.002605(80)	0.001253(42)	0.000775(24)	0.000393(12)	0.000268(8)	-	-	-
M	0.003607(111)	0.003703(114)	0.003409(105)	0.002651(81)	0.001348(45)	0.000859(27)	0.000439(13)	0.000297(9)	-	-	-
N	0.003832(118)	0.004125(127)	0.003639(112)	0.002637(81)	0.001873(62)	0.000717(22)	0.000331(10)	0.000223(7)	-	-	-
O	-	-	-	-	-	0.001490(74)	0.000932(46)	0.000702(35)	0.000569(28)	0.000505(25)	0.000382(19)
P	-	-	-	-	-	0.001689(83)	0.001125(55)	0.000854(42)	0.000689(34)	0.000619(30)	0.000473(23)
Q	-	-	-	-	-	0.001387(68)	0.000887(44)	0.000685(34)	0.000552(27)	0.000496(24)	0.000386(19)
R	-	-	-	-	-	0.001624(80)	0.001061(52)	0.000806(40)	0.000653(32)	0.000586(29)	0.000444(22)
S	-	-	-	-	-	0.001510(75)	0.000966(47)	0.000729(36)	0.000598(29)	0.000534(26)	0.000402(20)
T	0.004126(127)	0.004247(131)	0.004068(125)	0.003142(96)	0.001553(52)	0.001006(31)	0.000511(16)	0.000349(11)	-	-	-

For the $(n, 2n)$ experiments, the efficiencies at particular γ-ray energies are required. Interpolating between measured points is problematic because the functional form of the efficiency is not well known. Estimates of the additional uncertainty introduced via a spline interpolation range from 1-8% depending on the γ-ray energy. Hence, the MCNP model discussed in Section 4.1.3 has been used for interpolation in place of some arbitrary interpolation. The uncertainties of this approach are also discussed there.

4.1.3   Interpolation and comparison with MCNP calculations

A good Monte Carlo transport model of the GEANIE array is an important element of this effort for several reasons, providing:

1. Verification that measured values are reasonable

2. Physically realistic approach to interpolate efficiency between measured values with a point source

3. An accurate model to calculate geometrical losses for the extended beam spot, as discussed in Section 5

In this section, an MCNP model is described and compared to the absolute peak efficiency measurements described above. The model is used to interpolate the measured peak values, and an uncertainty in this procedure is estimated.

Only those items relevant to the full-energy, or peak, efficiency have been included in the MCNP model: the detector crystals, Be windows, and lead collimators. The NaI cones may be added in the future since they also play a small role in attenuating source photons. A cross-sectional view of the MCNP model is shown in Fig. 7. The input file for MCNP is listed in Appendix B.

Because of the sensitivity of the calculation to the array geometry, considerable effort has been made in the physical setup of GEANIE to reduce the MCNP input parameter space as much as possible. A lot of attention has been paid to aligning the detectors, collimators, target, and beam spot to within 3 mm of a central point. All the relevant physical dimensions have been measured to better than ± 1 mm, and the angular position of the detectors with respect to the target have been measured to within 2°. Initially, the Ge crystal and Be window geometries were obtained from the Ortec spec sheets. The results of this initial MCNP calculation is compared to the measured efficiency in Figure 8. The agreement at this stage is remarkably good, considering that no attempt has been made to optimize the calculation by varying the MCNP input parameters.

The MCNP parameters which are most uncertain are those describing the Ge crystal geometries. The side and back edges of these crystals have sizeable dead layers which vary from detector to detector. The back dead layer has been estimated by comparing the shape of the measured efficiency curves to those predicted by MCNP. To estimate the size of the side dead layers, source measurements have been made with the point source on the front face of the lead collimators. These "uncollimated" measurements are more sensitive to the surface area presented by the detector crystal, because the lead collimators shadow the crystal somewhat
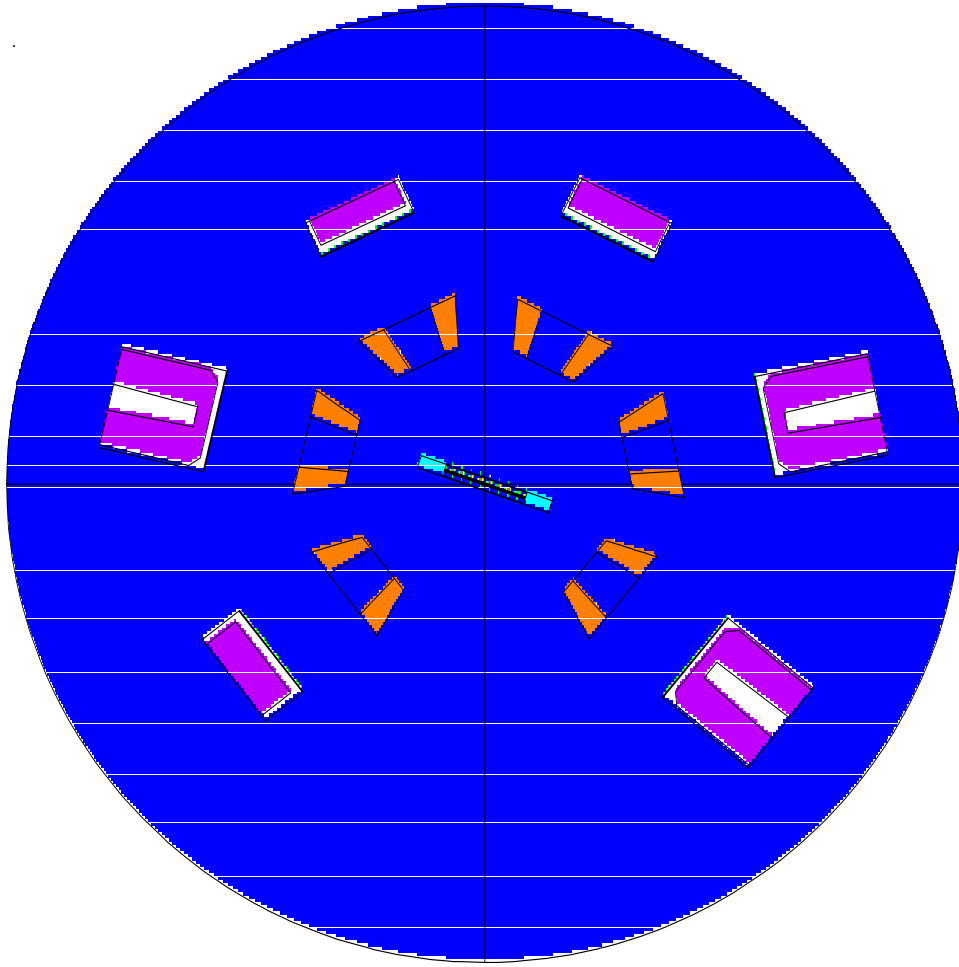
Figure 7: The plotm file from MCNP for a cross-sectional view of the array from the top. The beam enters the array from the bottom of the figure. The detectors in the figure clockwise from left of beam are T, Q, N, K, H, and E.
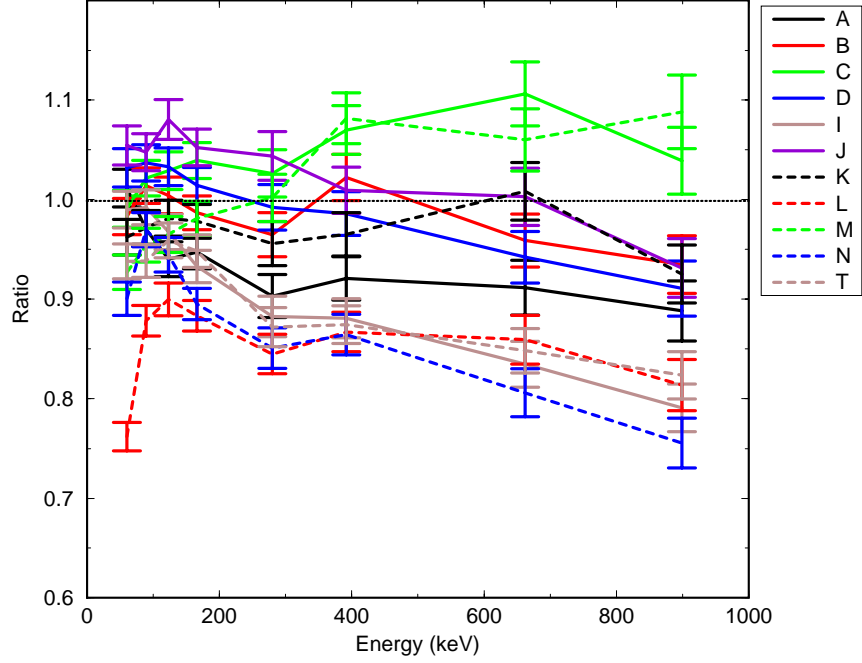
Figure 8: Initial results of MCNP model of the centered point source measurement. The ratio of the measured to calculated photopeak efficiencies is plotted for several γ-ray source energies. Only the results for the planar detectors are shown here. A ratio of 1.0 implies that the measurement and calculation agree.

when the point source is at the center of the array. In addition, the collimator-to-center distances have also been varied within measurement error to get better agreement. The initial and final MCNP crystal parameters are summarized in Table 12. Improvements have been made to planar detectors only. The coaxial detectors have more features, which discourages this extra effort. In fact, further iterations on the changes to the planar crystals would improve the results, but the actual gain in usefulness for our purposes would be minor.

The results of these improved calculations are compared to the point source measurements in Figure 9. Except for Detector L, the agreement between calculation and measurement is quite good, especially for γ-ray energies below about 250 keV.

With this MCNP model in hand, it can be used to do realistic interpolations between measured values. For an efficiency, ε, at energy E' which lies between measured energies E_1 and E_2, the interpolated efficiency is given by:

$$\varepsilon(E') = \frac{1}{2}\left[\varepsilon(E_1)\frac{\varepsilon_{MCNP}(E')}{\varepsilon_{MCNP}(E_1)} + \varepsilon(E_2)\frac{\varepsilon_{MCNP}(E')}{\varepsilon_{MCNP}(E_2)}\right] \tag{13}$$

Table 12: For each detector, the values of parameters used for the initial (I) and final (F) MCNP calculations. These parameters include center to collimator distances, center to Be window distances, Ge crystal length, and Ge crystal diameter. All distances are in millimeters with uncertainties of ±1 mm.

| Detector		Ge Length		Ge Diameter	
		I	F	I	F
1	A	17	15.0	51	46.2
2	B	20.4	18.9	51	48.4
3	C	18.4	17.9	51	47.2
4	D	18.4	18.4	51	46.6
5	E	54.6	54.6	50.9	50.9
6	F	51.0	51.0	48.8	48.8
7	G	47.5	47.5	50.3	50.3
8	H	56.9	56.9	50.9	50.9
9	I	19.0	18.0	51	49.2
10	J	17	17.0	51	48.2
11	K	17	17.0	51	51.0
12	L	17	16.5	51	48.8
13	M	17	19.0	51	48.0
14	N	15.5	14.0	51.0	48.8
15	O	54.2	54.2	49.9	49.9
16	P	59.0	59.0	48.7	48.7
17	Q	52.9	52.9	51.0	51.0
18	R	55.7	55.7	50.5	50.5
19	S	52.7	52.7	49.3	49.3
20	T	20	19.5	51	47.0
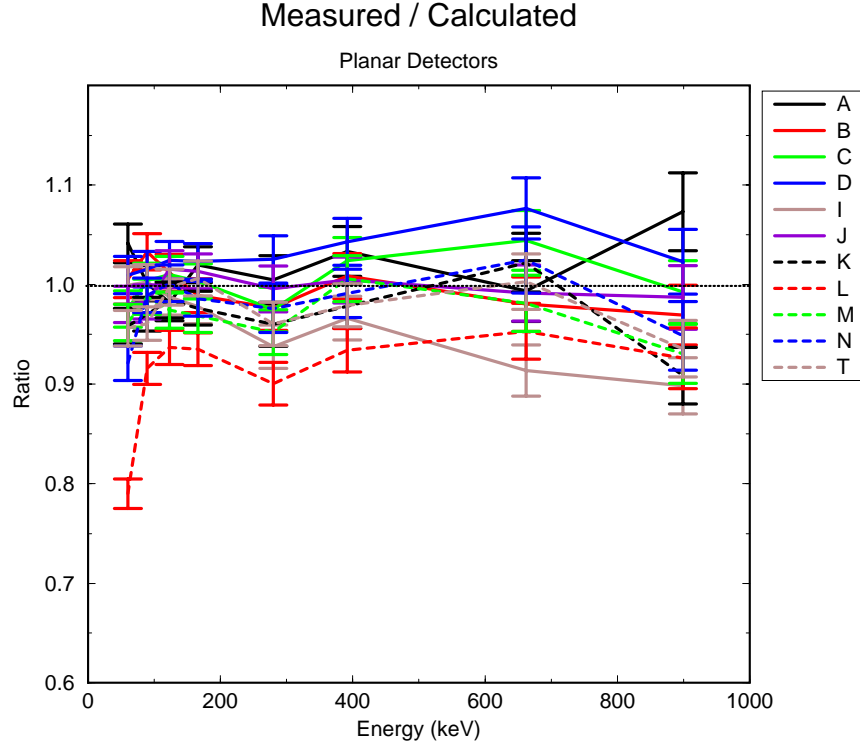
Figure 9: Final results of the MCNP model of the centered point source measurement. The ratio of the measured to calculated photopeak efficiencies is plotted for several γ-ray source energies. Only the results for the planar detectors are shown here. A ratio of 1.0 implies that the measurement and calculation agree.

where ε_{MCNP} is the efficiency calculated by MCNP. The uncertainty in this approach can be estimated by using the procedure to try to reproduce the measured efficiency of a peak by using two nearby source lines. The interpolation procedure is able to reproduce the measured efficiency with a statistical uncertainty of 1.8%. The interpolation procedure has been carried out for 10 keV steps from 60 keV to 890 keV for the planars, from 300 keV to 1800 keV for the coaxial detectors. The results are shown in Figure 10 and can be found on dollar.llnl.gov in /home/mcnabb/efficiency/pteff/evaluated.dat. The files coaxsum.dat and planarsum.dat in the same directory contain, obviously, the sum of the efficiencies over the coaxes and planars, respectively. The subdirectory interpolation contains the files used to do the interpolation.

4.2 Deadtime correction procedure

Deadtime is the probability that a pulse height in a detector is *not* histogrammed offline. Livetime is the probability that a pulse height in a detector *is* histogrammed offline. Livetime, T_{live}, is determined by taking the ratio of the number of Compton-suppressed pulse heights histogrammed offline to the number of Compton-suppressed pulse heights induced in the detector. The Compton-suppression consists of BGO crystals encircling the detector plus a cone-
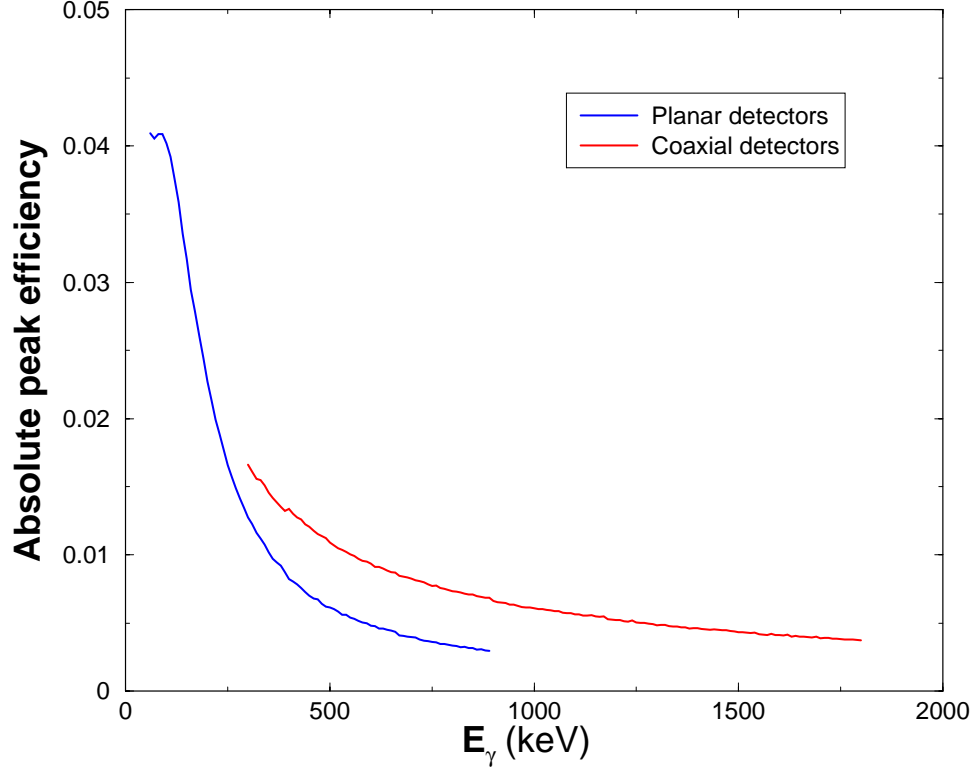
Figure 10: The absolute peak efficiencies for a point source is plotted for the planar detectors and the coaxial detectors. Error bars are not included but are discussed in the text. More detailed information can be found in the text.

shaped NaI crystal that extends beyond the front face of the Ge detector crystal. Suppression occurs when either the BGO or NaI records a pulse height in coincidence with the detector crystal. Such a coincidence implies that the full energy of γ ray was not absorbed in the Ge crystal. The number of Compton-suppressed pulse heights induced in the detector is determined by scaling the fast timing signal for these events on a detector-by-detector basis. These scalers will be called the "Compton-suppressed" scalers. An important point is that the scalers have essentially no deadtime. The scalers have a double pulse resolution time of < 30 ns, and therefore, can sustain rates of up to 30,000 counts per second with a deadtime of $< 0.1\%$.

In this discussion, the focus is on γ-ray detectors, but the discussion applies equally to the neutron flux monitors. Deadtime differences due to higher rates in the γ counters are captured by our procedure.

During the offline analysis the number of counts recorded to tape for each detector, or "ADC" channel counts, is determined. *The ratio of ADC counts to Compton-suppressed counts, is an accurate measure of the percentage livetime during the experiment.* The quantity N/T_{live}, where N is the number of counts in a photopeak, is compared directly to the product of source strength and the duration of the measurement. During an in-beam measurement, the number of counts observed in a photopeak N is compared to the measured neutron flux. In this case, the ratio of T_{live} for the γ-ray detector to T_{live} for the neutron flux monitor is the relevant

quantity. The flux monitor rate is ≈ 1 Hz. Therefore, T_{live} for the neutron flux monitor is expected to be dominated by the deadtime of the acquisition system. The γ-ray detector rates are often dominated by target radioactivity and are significantly higher.

4.2.1 Validation of measured deadtime

An attempt has been made to systematically break down the deadtime into its constituent parts, e.g. pileup, and to independently estimate each part of the deadtime by using rates and manufacturer-specified electronic deadtimes. This has not only helped to validate our procedure, but was also a useful debugging tool. In addition, as part of the validation procedure, several tests have been performed with the same experimental arrangement, but different deadtimes, in order to verify that the measured efficiency of the GEANIE array is not dependent on rate, pileup, and other factors which contribute to deadtime. These test measurements are discussed in Sections 4.2.2 and 4.1.2.

The deadtime has been broken down into four components:

1. System is dead for readout (almost measured by pulser)

2. Events lost in hardware or software (lost buffers, bad events, etc)

3. Pileup rejection

4. Channel of ADC is dead for conversion or readout

Each component is separately estimated below. System effects were independently measured with scalers. Pileup rejection is considered as a special paralysable system and channel deadtime is considered as a standard nonparalysable system (See [Kno79] for a discussion of paralysable and nonparalysable systems). In each case, some sample numbers are included which all come from the same calibrated point source measurement. This particular measurement had a time-averaged array rate similar to the plutonium measurement.

System is dead for readout
There are two types of "Compton-suppressed" scalers: (1) "Compton-suppressed, not busy" which scales Compton-suppressed signals when the system is not busy and (2) "Compton-suppressed, all" which totals the number of Compton-suppressed signals. A fixed-rate pulser, which generates a detector-like pulse, is used as a diagnostic. The pulser signal is treated like the other detector signals electronically. The ratio of the number of "Compton-suppressed, not busy" pulser counts to the number of "Compton-suppressed, all" counts measures the percentage of time the system was alive (not reading out) when a pulser signal arrived. Note, the pulser generates deadtime for the other channels = (24 μsec) × (Pulser conversions). Hence, the following statement should be true: (Detector Compton-suppressed, not busy)/(Detector Compton-suppressed, all) = $(1 -$ (24 μsec) × (Pulser conversions)) × (Pulser Compton-suppressed, not busy) /(Pulser Compton-suppressed, all). One should note that the percentage of time that the system is alive should be the same for all detectors. In a typical point source measurement, we get the following output from EFFICIENCY.PL for each detector:

```
-->System livetimes:
Detector        Estimated       Measured
   1              0.887           0.892
   2              0.887           0.890
   3              0.887           0.892
   4              0.887           0.892
   5              0.887           0.892
   6              0.887           0.889
   7              0.887           0.892
   8              0.887           0.892
   9              0.887           0.889
  10              0.887           0.891
  11              0.887           0.869
  12              0.887           0.892
  13              0.887           0.892
  14              0.887           0.892
  15              0.887           0.892
  16              0.887           0.891
  17              0.887           0.891
  18              0.887           0.892
  19              0.887           0.892
  20              0.887           0.892
  30              0.887           0.893
  31              0.887           0.880
```

where detectors 30 and 31 are the neutron flux monitors. Except for Detector 11(K), all livetimes are consistent with expectations within 1%, an estimate of uncertainty for this component. This analysis pointed to problems with the Detector Compton-suppressed scaler for Detector 11. We suspect that this was due to a bad cable which causes intermittent double pulsing due to reflections. The estimated deadtime was used in place of the measured deadtime for Detector 11 during the analysis.

Events lost in hardware or software
Because the pulser signal is never Compton-suppressed, it might be expected that the pulser's ADC counts would equal pulser's "Compton-suppressed, not busy" scaler. This is not the case because (1) converted pulses are not recorded to tape properly (e.g. lost buffers or bad events), (2) some Compton-suppressed pulses are not properly converted and readout by the ADC, or (3) the analysis software does not read the tape properly. Bad events and bad buffers have been observed and are apparently due to events being misaligned in the histogrammer module. This deadtime is rate dependent, with more deadtime at higher rates. If this unexplained deadtime was due to random mishaps in the histogrammer module then the pulser measures the percentage of lost counts for all detectors: ((Pulser Compton-suppressed, not busy) − (Pulser counts))/(Pulser Compton-suppressed, all).

However, significant differences can occur between detectors that pileup rejection and other effects discussed below cannot account for. Typical numbers for this deadtime is shown here:

```
Percentage losses due to lost events:
-->Pulser: 0.084
-->Det  1: 0.118
-->Det  2: 0.102
-->Det  3: 0.086
-->Det  4: 0.085
-->Det  5: 0.130
-->Det  6: 0.089
-->Det  7: 0.097
-->Det  8: 0.091
-->Det  9: 0.093
-->Det 10: 0.085
-->Det 11: 0.119
-->Det 12: 0.096
-->Det 13: 0.093
-->Det 14: 0.086
-->Det 15: 0.126
-->Det 16: 0.120
-->Det 17: 0.106
-->Det 18: 0.094
-->Det 19: 0.111
-->Det 20: 0.091
-->Det 30: 0.092
-->Det 31: 0.094
```

It is apparent that the detector losses are always larger than the losses expected on the basis of the pulser. A valid concern is that the CFD thresholds are set lower than the ADC lower-level discriminators. As discussed above in Section 4.1.2, this would result in an overestimate of the deadtime since the ADC would fail to convert Compton-suppressed, low-energy pulses. However, the CFD thresholds were set at conservative high values for this measurement and so this possibility is excluded. Therefore, these losses probably arise elsewhere in the hardware or analysis software.

Further evidence that these losses are real, and are well-reproduced by the deadtime correction procedure is available from a high-rate test, discussed below in Section 4.2.2. At higher rates this discrepancy between the pulser and the individual detectors grows, however, the deadtime correction procedure still correctly reproduces the measured efficiency within about 2%, which serves as an estimate of the uncertainty from this component of the deadtime.

Pileup rejection

In this system, pileup occurs when two pulses arrive in a gated integrator within 10 μsec of each other. Both pulses are lost. The pileup rejection circuitry is paralysable, i.e. a third pulse

will be lost if it comes within 10 μsec of the second. Hence, pileup deadtime is $2(1 - e^{-n/\tau})$ where n is the raw rate of the detector and $\tau = 10$ μsec. Pileup losses with our counting rates are typically small, on order of 1%. However, tests have been run at higher rates when pileup is as high as 10%, and this estimate of pileup is accurate. Here is a sample output from EFFICIENCY.PL for each detector:

```
-->Percentage losses due to pileup:
Detector  Percentage loss
   1               0.011
   2               0.011
   3               0.011
   4               0.011
   5               0.002
   6               0.002
   7               0.002
   8               0.002
   9               0.010
  10               0.011
  11               0.003
  12               0.010
  13               0.009
  14               0.010
  15               0.002
  16               0.002
  17               0.002
  18               0.002
  19               0.002
  20               0.011
  30               0.000
  31               0.000
```

Channel of ADC is dead for conversion

This is additional channel deadtime which is not accounted for as system deadtime or pileup. In this instance, the ADC channel is already converting or waiting for readout when the second pulse arrives. The ADC master gate is 20 μsec per event. However, due to internal circuitry requirements, only 17.6 μsec are available for conversion. The first 10 μsec, will result in pileup, so the only additional deadtime occurs in the last 7.6 μsec. Hence, (Detector Compton-suppressed rate)$\times$(7.6 μsec) is the overall deadtime correction here. Clearly, this correction is smaller than the 1% pileup correction given above.

Other effects — false suppression, summing

In order to compare efficiency measurements to calculations, one must also account for false suppression by the BGO and NaI Compton shields. This correction is is not discussed here because it is on order of 0.1% during the $(n, 2n)$ experiments. However, this effect is calculated

in EFFICIENCY.PL as a check. Likewise, summing is negligible. Individual detectors have a maximum photopeak efficiency of about 0.003. Assuming an event multiplicity of 10 γs implies a summing correction on order of 0.05%.

Summary

The overall deadtime correction as estimated for these four components is compared to the measured deadtime in the output of EFFICIENCY.PL. This comparison is presented here for the example we have been following:

```
-->Overall livetimes:
Detector  Estimated  Measured
    1            0.774        0.774(0.000)
    2            0.788        0.786(0.000)
    3            0.802        0.802(0.000)
    4            0.803        0.803(0.000)
    5            0.772        0.773(0.001)
    6            0.810        0.809(0.001)
    7            0.802        0.803(0.001)
    8            0.808        0.809(0.001)
    9            0.796        0.794(0.000)
   10            0.804        0.803(0.000)
   11            0.782        0.763(0.001)
   12            0.795        0.795(0.000)
   13            0.798        0.798(0.000)
   14            0.803        0.803(0.000)
   15            0.776        0.777(0.001)
   16            0.781        0.781(0.001)
   17            0.795        0.795(0.001)
   18            0.805        0.806(0.001)
   19            0.790        0.791(0.001)
   20            0.798        0.797(0.000)
   30            0.808        0.811(0.007)
   31            0.807        0.797(0.018)
```

As described above, the deadtime correction procedure of taking the ratio of ADC counts to "Compton-suppressed" counts as the livetime can be estimated by breaking the deadtime down into its constituent parts. In order to validate this procedure further, other tests have been performed and are thoroughly discussed in Section 4.2.2. The main conclusion of these additional tests is that the deadtime correction procedure consistently reproduces the same efficiency within about 3% under a variety of deadtime scenarios. This serves as an estimate of the uncertainty in the deadtime correction procedure.

4.2.2 Tests of the deadtime correction procedure

The deadtime correction procedure has been tested by measuring the point source efficiency of the GEANIE array with different deadtime scenarios and with several different scaler readout intervals. The latter set of tests was done because it was noted that the frequency with which the data acquisition freezes (locks up) increases as the scaler readout interval is modified. The reason for this behavior is that the scaler readout bus and detector readout bus are independent of each other and do not handshake. As the readout interval was increased, it became more likely that the data buffering had not completed reading out when the scaler buffer readout occurred, which resulted in a freeze-up. It was verified that large swings in scaler rates did not occur over readout interval timescales [You99]. This would occur, for example, if there was a noise source which caused many pulses at the scaler input.

The first test was to change the scaler readout time from 4 seconds to 2 seconds. The ratio of the efficiency measured in this test to the canonical efficiency measurement is shown in Figure 11. The ratio is consistent with 1 and shows a scatter of 0.4%, which is consistent with statistical uncertainties.

However, when the scaler readout time was changed to 40 seconds, problems occurred with some detectors. The results of this measurement are compared to the canonical measurement in Figure 12. This problem has again been traced to the Compton-suppressed, all scaler. The number of scaled counts recorded in the data on tape is too large for the detectors which are not in agreement. It is not clear whether this result is anomalous or related to the long readout times.

The third test involved setting the pulser to 15 kHz. This increased the detector deadtimes from about 20% to about 70%. The results, shown in Figure 13, are in reasonable agreement with the canonical measurement, though there are clearly some effects on the order of 2% which are not understood. One possibility is that the measured deadtime is too large.

In conclusion, the measured deadtime rates appear to be reasonably consistent as the scaler readout time is changed. The data acquisition freezes every few minutes when the scaler readout time is set to 40 seconds. Perhaps the reason for the anomalous results and the freeze-ups are related. Also, the 15 kHz test suggests that the measured deadtimes are trustworthy at an approximate 2% level.

4.2.3 In-beam deadtime correction and uncertainty

Deadtime corrections in the analysis of in-beam data differ from that of source data in that the γ-ray counts in an in-beam measurements are normalized to neutron flux instead of source strength. An important consideration in the deadtime correction procedure is that the neutron flux monitors use the same electronics and acquisition as the GEANIE array. For example, the coaxial, planar, and fission chamber amplifiers are all Tennelec 245 modules with identical triangular shaping times of 3 μs. Not only does this ensure that the deadtime correction procedure is the same for γs and neutrons, but they also have similar deadtimes.

Another consideration is whether there are any neutron TOF-dependent deadtime effects. In beam, the probability an individual γ detector (beam-induced rate < 1000 Hz) will register a pulse height per incident proton pulse driving neutron production (rate ≈ 35000 Hz) is less
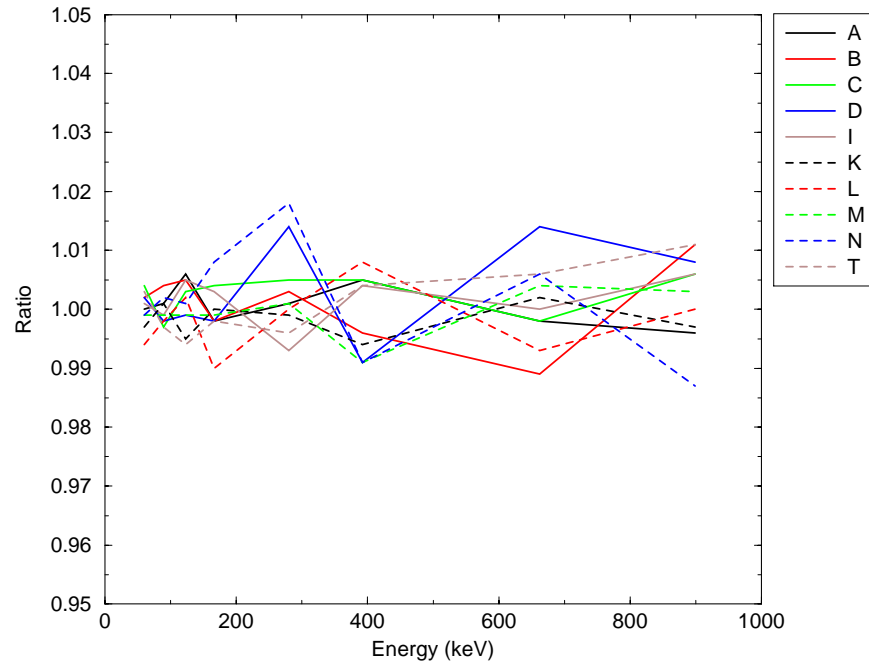
Figure 11: Ratio of efficiency measured with a 2-second scaler readout interval compared with the canonical 4-second interval measurement.
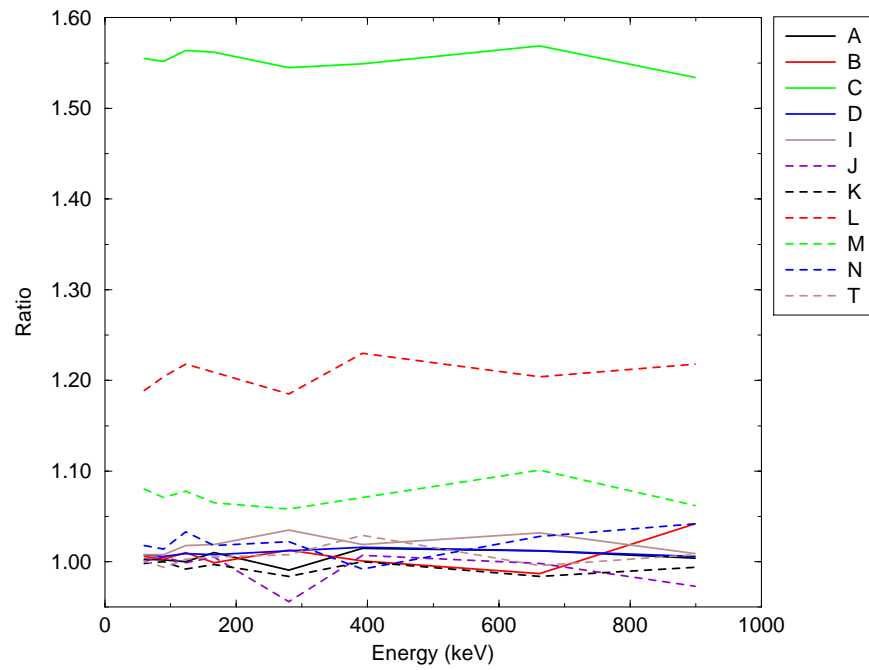

Figure 12: Ratio of efficiency measured with a 40-second scaler readout interval compared with the canonical 4-second interval measurement.
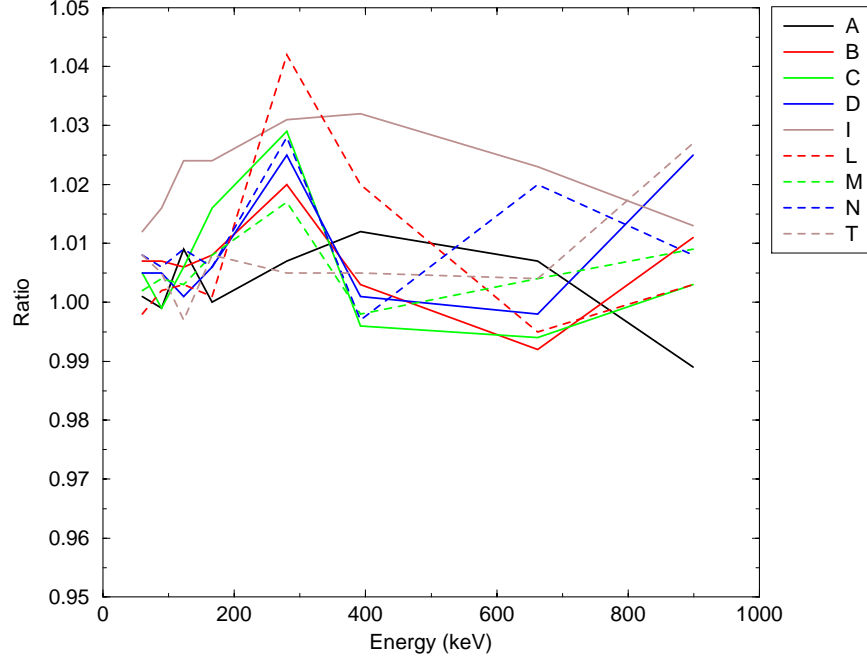
Figure 13: Ratio of efficiency measured when the array rate was set artificially high by using a pulser set to 15 kHz compared with the canonical measurement, which has a typical array rate of about 3 kHz.

than 3%. Hence, the probability a detector will register two pulses from the same proton pulse is negligible ($< 1\%$). If this probability was non-negligible, then the second γ ray would be detected less efficiently than the shorter-TOF γ ray because the second *gamma*-ray would be discarded by the electronics. This effect can be monitored by inspecting the TOF spectra of target radioactivity. Within statistics these TOF spectra are flat, hence, there is no appreciable change in efficiency as a function of neutron TOF. Therefore, neutron TOF-dependent deadtime effects are not considered.

The main difference in deadtime between the GEANIE array and the neutron flux monitors arises from different detector rates. Since the rates in the flux monitors are much lower than the Ge detectors rates, we would expect that the flux monitors to be alive a greater fraction of the time. The livetime correction factor for the ratio $\frac{N_\gamma}{\Phi}$ (see Equation 8) is given by

$$\left(\frac{\text{(Monitor conversions)}}{\text{(Monitor Compton-suppressed scaler)}} \right) \left(\frac{\text{(Detector Compton-suppressed scaler)}}{\text{(Detector conversions)}} \right) \quad (14)$$

Table 13 lists this correction factor for each detector for both flux monitors for the $^{235}\text{U}(n, 2n)$ and $^{239}\text{Pu}(n, 2n)$ measurements. The numbers in this table and in the discussion below are derived from preliminary values obtained from Walid Younes [You99] for ^{235}U and from Lee Bernstein [Ber99] for ^{239}Pu.

To give the reader a better understanding of the deadtime scenario, and hence where the correction factors listed in Table 13, a complete listing of the deadtime components as discussed

above in Section 4.2.1 is given for the worst-case in-beam measurement — the 20-mil ^{239}Pu target. For brevity, only the output for the planar detectors and the flux monitors (Detectors #30 and #31) is listed.

```
-->System livetimes:
Detector        Estimated       Measured
   1             0.592           0.593
   2             0.592           0.592
   3             0.592           0.593
   4             0.592           0.592
   9             0.592           0.592
  10             0.592           0.593
  11             0.592           0.593
  12             0.592           0.592
  13             0.592           0.592
  14             0.592           0.592
  20             0.592           0.592
  30             0.592           0.590
  31             0.592           0.589


-->Percentage losses due to pileup:
Detector        Percentage loss
   1             0.197
   2             0.205
   3             0.181
   4             0.180
   9             0.204
  10             0.207
  11             0.269
  12             0.251
  13             0.260
  14             0.248
  20             0.202
  30             0.001
  31             0.000


-->Leftover channel deadtime:
Detector        Percentage loss
   1             0.047
   2             0.047
   3             0.042
   4             0.042
   9             0.044
```

```
10                   0.046
11                   0.053
12                   0.050
13                   0.052
14                   0.046
20                   0.049
30                   0.000
31                   0.000
```

```
Percentage losses due to lost events:
-->Det  1: 0.183
-->Det  2: 0.165
-->Det  3: 0.188
-->Det  4: 0.182
-->Det  9: 0.194
-->Det 10: 0.168
-->Det 11: 0.145
-->Det 12: 0.207
-->Det 13: 0.185
-->Det 14: 0.151
-->Det 20: 0.206
-->Det 30: 0.297
-->Det 31: 0.317
```

```
-->Overall livetimes:
Detector          Estimated          Measured
   1                0.368           0.340(0.000)
   2                0.375           0.345(0.000)
   3                0.374           0.349(0.000)
   4                0.379           0.353(0.000)
   9                0.360           0.330(0.000)
  10                0.371           0.343(0.000)
  11                0.350           0.315(0.000)
  12                0.334           0.292(0.000)
  13                0.337           0.298(0.000)
  14                0.361           0.329(0.000)
  20                0.354           0.321(0.000)
  30                0.416           0.414(0.001)
  31                0.404           0.402(0.001)
```

In this particular experiment, the effects of target radioactivity which result in higher detector rates can be seen in the large system deadtime ($\approx 40\%$) and the large pileup rejection rates ($\approx 20\%$). The measured deadtime correction factor for Detector 1 (or A) when normalized to

Flux monitor #1 (the ^{235}U fission chamber), is given by $0.414/0.340 = 1.218$. The estimated value, on the other hand, would be $0.416/0.368 = 1.129$. These values are reflected in Table 13.

Table 13: Deadtime correction factors for the ^{235}U$(n, 2n)$ and ^{239}Pu$(n, 2n)$ measurements.

Det.	Flux monitor #1	Flux monitor #2	Estimate #1	Estimate #2
^{235}U 12-mil target			
1	1.057	1.042	1.052	1.032
2	1.061	1.046	1.054	1.034
3	1.051	1.036	1.047	1.027
4	1.046	1.032	1.043	1.023
9	1.105	1.090	1.090	1.070
10	1.073	1.058	1.062	1.041
11	1.144	1.127	1.113	1.092
12	1.173	1.157	1.139	1.118
13	1.162	1.146	1.130	1.108
14	1.104	1.088	1.080	1.060
20	1.089	1.073	1.079	1.059
^{235}U 24-mil target			
1	1.114	1.067	1.080	1.057
2	1.109	1.062	1.074	1.052
3	1.104	1.057	1.073	1.051
4	1.089	1.043	1.062	1.040
9	1.229	1.177	1.165	1.141
10	1.137	1.089	1.095	1.073
11	1.262	1.208	1.185	1.160
12	1.307	1.251	1.215	1.189
13	1.300	1.245	1.212	1.187
14	1.189	1.139	1.134	1.110
20	1.174	1.124	1.120	1.097
^{239}Pu 10-mil target			
1	1.150	1.121	1.093	1.065
2	1.138	1.109	1.086	1.058
3	1.131	1.102	1.083	1.056
4	1.123	1.094	1.073	1.046
9	1.181	1.150	1.115	1.086
10	1.149	1.119	1.090	1.063
11	1.221	1.190	1.139	1.110
12	1.310	1.276	1.205	1.175
13	1.283	1.250	1.180	1.150
14	1.190	1.159	1.118	1.089
20	1.200	1.169	1.129	1.101

continued from previous page

Det.	Flux monitor #1	Flux monitor #2	Estimate #1	Estimate #2
^{239}Pu 20-mil target				
1	1.218	1.182	1.129	1.098
2	1.198	1.163	1.109	1.079
3	1.186	1.151	1.110	1.080
4	1.172	1.138	1.097	1.067
9	1.255	1.218	1.153	1.122
10	1.206	1.171	1.119	1.088
11	1.312	1.274	1.188	1.155
12	1.419	1.377	1.243	1.208
13	1.390	1.349	1.232	1.198
14	1.258	1.221	1.153	1.121
20	1.288	1.251	1.175	1.143

By comparing Columns 2 and 4 in Table 13, for example, it can be seen that the estimated values of the deadtime correction factor do not completely agree with the measured value. On average the 12-mil ^{235}U has differences of about 2%, the 24-mil ^{235}U has differences of about 4%, the 10-mil ^{239}Pu has differences of about 7%, and the 20-mil ^{239}Pu has differences of about 11%. It appears that the detectors with the highest rates have the largest discrepancies.

4.3   Summary

In summary, the absolute peak efficiencies for a point source have been measured for 11 γ-ray energies from 60-1900 keV. These measurements are in reasonable agreement with MCNP calculations. For each detector there is a statistical $\approx 3\%$ experimental uncertainty in the efficiencies due to uncertainty in the source placement. This uncertainty averages out to about 1% when the planar detectors are summed. The source strength contributes an overall systematic uncertainty of about 1.5%. The vendor-provided values of the source strength have been validated by a calibrated measurement at LLNL. Interpolation between measured values has been done with a MCNP calculation and a statistical uncertainty of about 2% for each detector has been ascribed to this procedure.

The deadtime procedure has been reasonably validated, however, the origin of some event losses are not completely understood. Several measurements of the point source efficiency have been made under different deadtime scenarios, verifying that the deadtime correction procedure reproduces the same values on a consistent basis.

5 Correction to efficiency for extended beam spot geometry

The γ rays emitted from the target are distributed according to the neutron beam profile which is approximately 0.5 inch in diameter. In this Section, the correction for geometrical effects which lower the efficiency for detecting γ rays from the edges of the beam profile is discussed. This exercise breaks down into two parts: (1) determining the neutron beam profile (Section 5.1), and (2) determining the geometrical correction arising from that profile (Section 5.2).

5.1 Neutron beam profile

The neutron beam profile was measured by exposing a Fuji image plate for one hour at a proton beam current of 1600 nA, with a repetition rate of 100 Hz, 625 microsecond beam gate width, and 1.8 microsecond pulse spacing [Nel99]. The image plate has photostimulable phosphor and the scanner used to read the image uses a laser to stimulate luminescence [Miy86, Nii94]. The image plate is sensitive to x-rays, so a copper plate was placed in front of the image plate to act as a converter. The dispersion of the image scan is 150 pixels per inch (6.7 mils). The quoted dynamic range of the image plate is 10^5.

A pinhole was used to align the image plate with the sample center position as defined by the sample holder and square frame. Alignment was checked with a transit. The uncertainty in centering is approximately 1 mm and in angular alignment is about 3°. The beam profile has been measured several times over the course of one year. No evidence of instability in the beam profile was observed.

Figure 14 shows a density plot of a typical image after it was digitized. Cuts on the image matrix were made through the center of the beam spot and are displayed in Figures 15 and 16. As is evident from these figures, the peak-to-halo ratio is at least 10^3. We were unable to get better dynamic range in the peak-to-halo ratio.

The correction factor can be fairly sensitive to beam profile, in particular the halo can have a large impact. There is more geometric phase space for neutrons further away from the beam center. The area of a ring about the center of width dr is rdr, i.e. is proportional to the distance from the center of the beam profile. Any part of the neutron halo which passes through the fission chamber is counted, but is less likely to result in an observed γ ray. The ratio of neutrons in the halo to those in the beam spot is $\lesssim 0.1\%$. Hence, the effects of the halo can be safely ignored.

In order to check that the measured beam profile is reasonable, Nelson [Nel00] has performed a ray tracing calculation to determine what the expected beam profile is based on our knowledge of the collimation in place. The resolution of this calculation is 0.1 inch per pixel. The result is displayed in Figure 17. Except for a difference in beam spot orientation, the main features of the calculated beam profile and measured beam profile are the same.
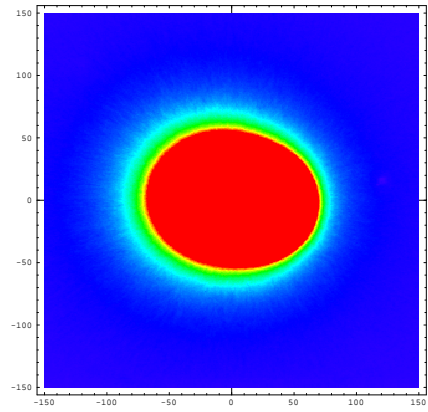
Figure 14: Density plot of beam profile in a downstream view. The figure is oriented so that gravity is the direction of negative ordinate.
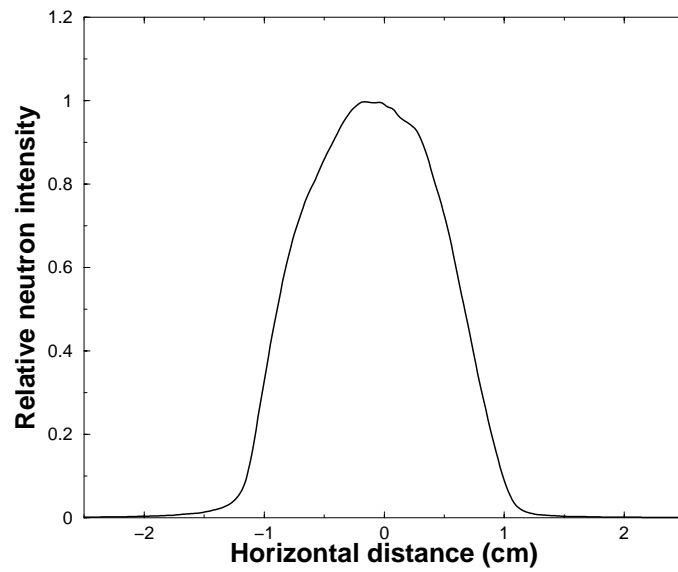

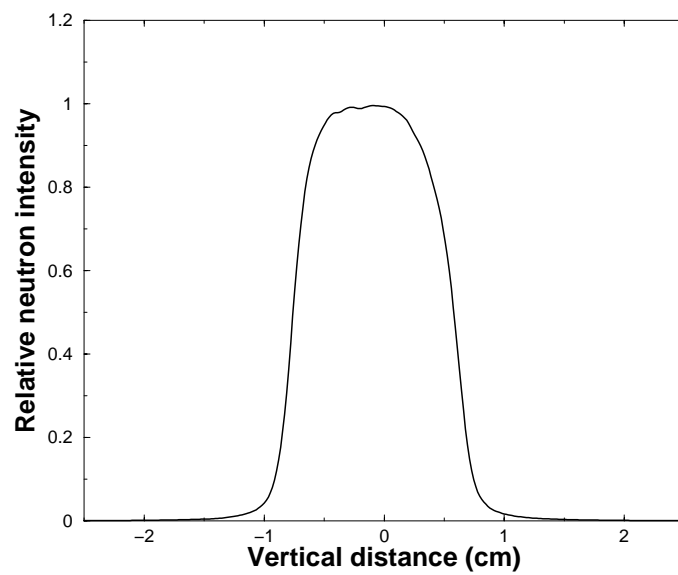
Figure 15: Line out of Figure 14 onto ordinate.

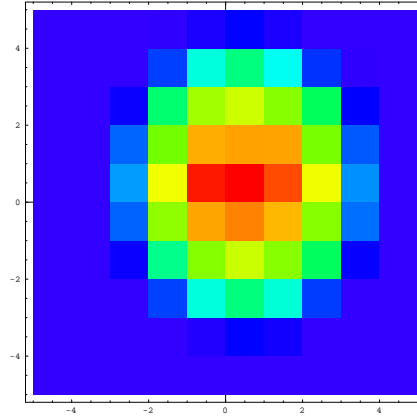Figure 16: Line out of Figure 14 onto abscissa.

Figure 17: Density plot of calculated beam profile in a downstream view. The figure is oriented so that gravity is the direction of negative ordinate.

5.2 Determining correction factor

The procedure used to determine the correction factor and its uncertainty is to use the MCNP model discussed in Section 4.1.3 to calculate the relative efficiency difference between a point source and the true beam profile. This approach was chosen over a direct measurement because of the difficulties encountered in obtaining a source which correctly mimicked the beam profile.

The beam profile and the efficacy of the MCNP model for reproducing the array performance for a point source has been well-documented in this paper. The remaining question is whether the MCNP model correctly describes how the efficiency changes as the source γ rays are emitted from an off-center point. A related question is "how good can we expect the MCNP model to do?" This goes right to the heart of the relative uncertainty in using this procedure to determine the correction factor.

Section 5.2.1 has a discussion of how good we can expect the MCNP model to work, an initial guess of the correction factor, and the results of applying the procedure including uncertainties. Section 5.2.2 presents the results of off-center point source measurements compared to MCNP calculations which serve as a stringent test of this procedure.

5.2.1 The geometrical correction and its relative uncertainty

As discussed in Sections 4.1.3 and 5.1, the relative position of the centerline of a particular detector and the array center is good to about 3 mm and the center of measured beam spot is is known to within 1 mm. The beam profile is about 17 mm in diameter. The uncertainty in the centerline of a particular detector matters less to the uncertainty in the extended correction than one might initially think. To determine the extended correction in the scenario that the centerline misses the defined array center by 3 mm, one would take the ratio of the MCNP

calculation for a point source off center by 3 mm to the MCNP calculation for the beam spot off center by 3 mm, rather than just investigating the effects of moving the beam spot by 3 mm.

To get a handle on what to expect, a series of MCNP calculations have been performed for rings of source material 0.1 inches in thickness. For example, the first calculation was for source material evenly distributed from $0 < r < 0.1$ in, the next calculation was for source material evenly distributed from $0.1 \text{in} < r < 0.2$ in, and so on. This allows us to get a handle on how the efficiency for detecting γ rays decreases as we move away from the array center. As discussed earlier in Section 5.1, the neutron flux increases as a function of r, the distance away from the center. In Figure 18, the neutron flux-weighted beam profile is overlayed with the MCNP calculation of the change in efficiency as a function of r.
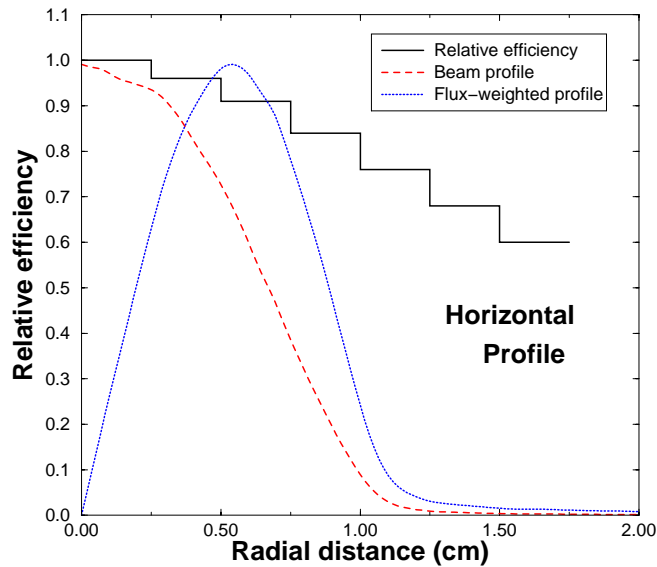
Figure 18: The relative efficiency (solid) as a function of r as calculated with MCNP is compared to the beam profile (dashed) and the flux-weighted beam profile (dotted). The majority of neutrons are located ≈ 5 mm from the center of the beam spot.

It is clear from the figure that the majority of neutrons are located ≈ 5 mm from the center of the beam spot. At this distance, the relative efficiency has decreased by $\approx 10\%$. Hence, we can expect that the geometric correction factor will be in the neighborhood of 10%. The results of MCNP calculations with the source material distributed with the measured beam profile are displayed in Figure 19 for each planar detector. It should be noted that there is some dependence on the γ-ray energy in the geometric correction factor.

From Figure 18, a 1 mm uncertainty in the peak of the neutron flux-weighted beam profile translates to $\approx 3\%$ uncertainty in the correction factor. However, as the peak moves away from the center in one radial direction, the peak in the opposite radial direction is moving closer. Therefore, we would expect some cancellation and that the uncertainty from this factor to be significantly less than 3%. MCNP calculations with the source material distributed with the measured beam profile bear this out, indicating that the uncertainty in the extended correction
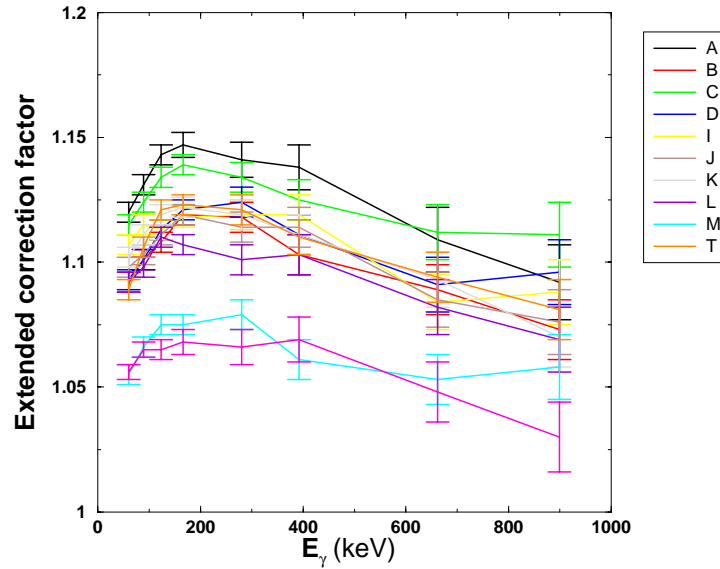
Figure 19: Extended correction factors as a function of E_γ, as calculated with MCNP for the planar detectors.

due to 1mm uncertainty in the location of the beam center is about 0.5%. However, the 3 mm uncertainty of the location of each detector's centerline contributes to a significantly larger uncertainty, and the MCNP calculations also indicate that the uncertainty is asymmetric. *The collection efficiency tends to decrease as the beamspot moves away from the centerline, favoring a larger correction.* The results of the full set of MCNP calculations, including the uncertainties derived from the off-center calculations are summarized in Table 14. The uncertainty is typically about 2% and have been estimated as described in Section 4.6 of [XCOM], i.e. it is assumed that 3 mm is the maximum deviation and that all values between 0 and 3 mm are equally probable. Also, the extended corrections have been calculated assuming that the centerline is $\approx$ 1.5 mm off-center. With this approach, it is reasonable to assume that the uncertainties quoted in are Table 14 symmetric.

5.2.2 Off-center point source measurements as a test of the procedure

In Section 5.2.1, the point was made that moving a detector's focal point away from the center of the beam spot by 3-4 mm, did not have a serious impact on the correction factor because as some parts of the beam moved away from the centerline, other parts of the beam moved toward the centerline. Off-center point source measurements are a more stringent test of the MCNP model because the efficiency is much more sensitive to changes in the point source position relative to the centerline.

Table 14: For each detector, the extended correction value at 60 keV and the relative uncertainty of the correction is listed. As discussed in the text, the main source of uncertainty arises from the 3 mm uncertainty in the location of the centerline of each detector.

Detector	Correction at 60 keV	Rel. uncertainty
1	1.138	0.021
2	1.110	0.021
3	1.128	0.017
4	1.106	0.017
5	1.101	0.016
6	1.080	0.014
7	1.059	0.015
8	1.075	0.013
9	1.114	0.013
10	1.112	0.018
11	1.114	0.016
12	1.107	0.018
13	1.065	0.015
14	1.078	0.025
15	1.049	0.015
16	1.057	0.015
17	1.013	0.013
18	1.061	0.016
19	1.051	0.017
20	1.105	0.019

Eighteen off-center point source measurements were made at six different offsets from the array center along three perpendicular axes. The offsets were approximately -15, -10, -5, 5, 10, and 15 millimeters from the array center. Because the centerline can be as much as 3 mm away from the center, we can only expect that MCNP will reproduce the results to that accuracy. For example, the ratio of the efficiency measured 5 mm from the array center to the efficiency measured at the center should be somewhere between the calculated ratio for 2 mm off center to 8 mm off center. This has been verified to be true for all the measurements.

6 Attenuation effects

In this section, the attenuation of γ-rays in the target is considered. The 100-250 keV γ rays observed in the (n,2n) experiments are significantly attenuated in the high-Z target material. Two different methods have been employed to calculate the attenuation correction: (1) analytically, with two simplifying assumptions and (2) using the MCNP model discussed previously in Section 4.1.3. These methods are in excellent agreement. As a result, the analytic approach is used in the data analysis because of its ease of use, particularly in propagating uncertainties in the target thickness and detector angle. The attenuation correction procedure described here has been verified experimentally by comparing results for targets of differing thicknesses.

6.1 Analytic approach

The attenuation of a photon beam is given by

$$I(x) = I_0 \exp(-\mu\rho x) \tag{15}$$

where I_0 is the incident beam intensity, μ is the density-independent attenuation coefficient, and x is the thickness of the absorbing material. Because the neutron beam is not significantly attenuated in the target, the emitted photons are distributed uniformly through the target thickness. Assuming (1) the finite solid angle subtended by each detector is small and (2) the beam spot is small compared to target-detector distance, it is safe to ignore the areal distribution of the beam profile. In this ideal case, the ratio of the number of *gamma* rays emitted from residual nuclei, $N_{\gamma_{emit}}$, to the number of emitted *gamma* rays that escape the target without being attenuated, $N_{\gamma_{escape}}$, (see term 2 of Eq. 8) is given by

$$\frac{N_{\gamma_{emit}}}{N_{\gamma_{escape}}} = \frac{\int_0^{l_{eff}} dx}{\int_0^{l_{eff}} \exp(-\mu\rho x)\, dx} = \frac{\mu\rho l_{eff}}{1 - \exp(-\mu\rho l_{eff})} \tag{16}$$

where $l_{eff} = t/\cos(\theta)$, the effective thickness of the target, θ is the detector-target angle and t is the target thickness.

Eq. 16, can be rewritten as

$$\frac{N_{\gamma_{emit}}}{N_{\gamma_{escape}}} = \frac{x}{1 - \exp(-x)} \tag{17}$$

where the parameter $x = \mu\rho t/\cos(\theta)$. For the purposes of understanding the uncertainties in $\frac{N_{\gamma_{emit}}}{N_{\gamma_{escape}}}$, it is not relevant how the uncertainties break down amongst μ, ρt, and θ. Instead we

are interested in σ_x/x, the relative uncertainty in x. The uncertainties in $\frac{N_{\gamma_{emit}}}{N_{\gamma_{escape}}}$ are given by

$$\frac{d\left(\frac{N_{\gamma_{emit}}}{N_{\gamma_{escape}}}\right)}{\frac{N_{\gamma_{emit}}}{N_{\gamma_{escape}}}} = \left| 1 - \frac{x \exp(-x)}{1 - \exp(-x)} \right| \frac{dx}{x} \tag{18}$$

Hence, the relative error x is weighted by a term which is always < 1. The weighting factor given in Eq. 18 is plotted as a function of x in Figure 20.

6.2 Discussion of relative uncertainties

In order to determine σ_x/x, values for σ_μ/μ, $\sigma_{\rho t}/\rho t$, and $\sigma_{\cos(\theta)}/\cos(\theta)$ have to be assigned. A discussion of the uncertainties in ρt can be found in Section 3, however, the ρt values used here are for all target constituents, *i.e.* the value before multiplying by the mass fraction. Currently, $\sigma_{\rho t}/\rho t = 0.91\%$ for the 20-mil plutonium target. The dominant sources of error in θ come from the alignment of the target with respect to the BGO shields ($1.5°$) and play of the detectors inside the BGO shields ($1.2°$). Hence the assumed error in θ is $2° = 0.0349$ radians.

The determination of σ_μ/μ is more complicated. Photon attenuation experiments have been carried out on plutonium and uranium [Con70, McC67] for selected energies from 25 keV to 3 MeV. These data points do not directly correspond to the $4^+ \rightarrow 2^+$ or $6^+ \rightarrow 4^+$ transition energies, and photo-attenuation cross sections vary rapidly in this energy region. Hence, we must rely on calculations. Table 15 compares data points with the XCOM data base at NIST [XCOM]. As can be seen from Table 15, agreement between calculation and experiment is not perfect. Using the 10 data points from 60.03 to 208.36 keV and adjusting for an overall systematic difference, it is necessary to introduce a 3.2% error in the calculation in order to enforce $\chi^2/\nu = 1$. This is in agreement with more sophisticated analyses by Storm and Israel [Sto70], Veigele [Vei73], and Saloman *et al.* [Sal88] where uncertainties of 3-5% are recommended. Hence, an inherent uncertainty of 3.2% in the values of μ derived from NIST calculations has been adopted. However, one other point to bear in mind is that the data tables in MCNP are binned, which introduces additional error in μ. The nominal uncertainty introduced by binning is $\leq 1\%$. Assuming an additional uncertainty of 1% in the lookup tables, $\sigma_\mu/\mu = 3.35\%$. Table 16 lists μ for transitions of interest, and the associated value of $\mu\rho t$ as determined for the thin and thick actinide targets in Section 3.

6.3 Comparison of analytic approach with MCNP model calculations

See Section 4.1.3 for a discussion of how the GEANIE array is modeled in MCNP. The only complication in MCNP is the determination of the relative uncertainty of the attenuation correction. The easiest approach is to vary the density of the target over the relative uncertainty in x in order to understand the uncertainties in this term. This approach is still valid even when the detector solid angle and beam spot are large, as long as these are modeled accurately in MCNP. The only drawback is that it doesn't capture the angular dependence of the uncertainty
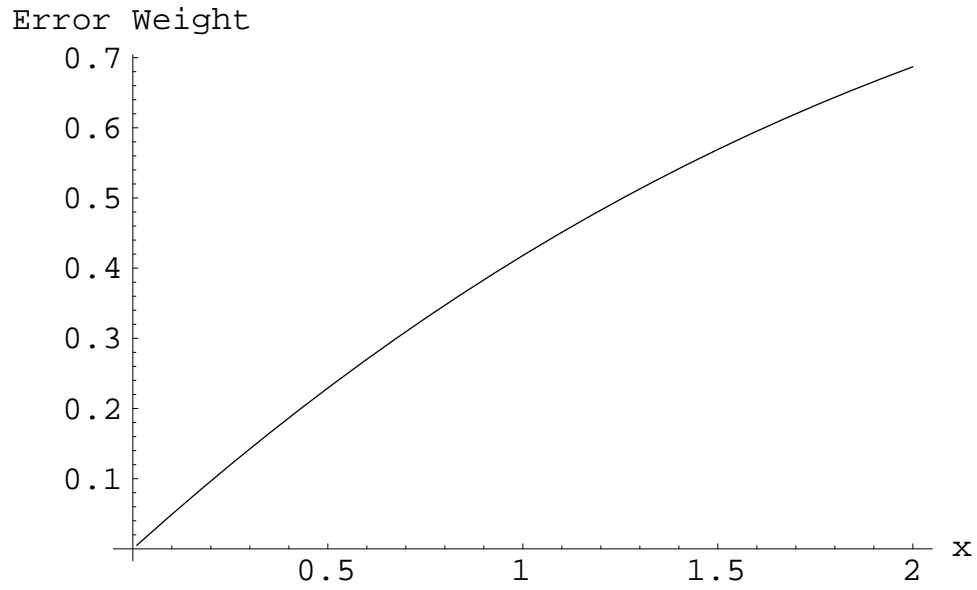
Figure 20: The weighting factor which relates the uncertainty in $\frac{N_{\gamma_{emit}}}{N_{\gamma_{escape}}}$ to the uncertainty in x, as a function of x.

Table 15: Comparison of measured photon attenuation coefficients (μ) in plutonium to calculations. Data taken from McCrary *et al.* [McC67] and Conner *et al.* [Con70]. Photon absorption calculations are interpolated tabular values from XCOM at NIST [XCOM].

Photon energy (keV)	Measured μ (cm^2/gm)	XCOM (cm^2/gm)
25.00(2)	67.5(1.3)	68.0
30.04(2)	42.98(64)	42.7
40.04(5)	21.77(20)	20.3
50.08(8)	11.70(15)	11.3
60.03(12)	7.40(10)	7.03
70.04(16)	4.953(81)	4.69
79.96(21)	3.543(24)	3.32
88.09	2.766(19)	2.58
89.92(26)	2.594(16)	2.45
100.06(32)	1.956(14)	1.86
109.99(39)	1.553(12)	1.82
130.31(55)	3.718(35)	3.72
145.41	2.929(12)	2.86
208.36	1.213(6)	1.19
279.12	0.6290(11)	0.607
411.80	0.2844(12)	0.275
661.6	0.1323(7)	0.129
1115.5	0.07176(31)	0.0706
1598.0	0.05404(17)	0.0543
2753.9	0.04549(22)	0.0459

Table 16: Adopted photon attenuation coefficients, μ, and associated values of $\mu\rho t$ for transitions of interest. The adopted attenuation coefficients are interpolated tabular values from XCOM at NIST [XCOM]. The ρt values are determined for thick and thin target configurations as discussed in Section 3. However, the ρt values used here are somewhat different in this case since all atoms in the target are included, not just the atomic fraction for the reaction of interest which is derived in Section 3.

Transition	μ (cm^2/gm)	$\mu\rho t$ (thick targets)	$\mu\rho t$ (thin targets)
^{238}Pu ($4^+ \rightarrow 2^+, 101.9$ keV)	1.78	1.410(49)	0.765(31)
^{238}Pu ($6^+ \rightarrow 4^+, 157.4$ keV)	2.34	1.854(64)	1.005(41)
^{238}Pu ($8^+ \rightarrow 6^+, 210.0$ keV)	1.17	0.927(32)	0.503(20)
^{234}U ($4^+ \rightarrow 2^+, 99.9$ keV)	1.71	1.842(120)	0.963(77)
^{234}U ($6^+ \rightarrow 4^+, 152.7$ keV)	2.36	2.542(165)	1.329(106)
^{234}U ($8^+ \rightarrow 6^+, 201.0$ keV)	1.21	1.303(85)	0.681(54)

in angle. In the comparisons done below, this uncertainty was not propagated through, because the additional work required was deemed unnecessary since the agreement with the analytic approach was so good.

Table 17 gives the assumed values of x, σ_x/x, $\frac{N_{\gamma_{emit}}}{N_{\gamma_{escape}}}$, and the relative uncertainty of $\frac{N_{\gamma_{emit}}}{N_{\gamma_{escape}}}$ for the 12-mil and 24-mil ^{235}U 1998 targets. The results of the analytic approach and MCNP calculations are included as a function of θ for angles which are relevant to GEANIE. The values presented Table 17 for the MCNP calculations compare well with the values derived from Eq. 16. The discrepancies are small and can largely be understood as statistical fluctuations in the MCNP calculation. The model for the monel ring in MCNP is fairly simple, so the $\frac{N_{\gamma_{emit}}}{N_{\gamma_{escape}}}$ values for the largest two angles should not be trusted. There is no monel ring included in the analytic approach, so the results for detectors Q, F, and G should not be used. The MCNP calculation of the relative uncertainty in $\frac{N_{\gamma_{emit}}}{N_{\gamma_{escape}}}$ is usually less than derived from Eq. 18. This is because the angular dependence of the effect of the 2° uncertainty in θ is not accounted for with the MCNP calculations.

Table 17: Values and uncertainties of term 2 of Eq. 8 are tabulated for each transition of interest in Table 16 as a function of GEANIE detector angle. Values and uncertainties derived from Eq. 16 are compared with those derived from MCNP calculations. The MCNP uncertainties are based on calculations where the density of the target was varied, as discussed in the text. MCNP calculations inherently include the effect the extended beam profile and close detector geometry. The planar detectors, which are the relevant detectors for the $(n, 2n)$ measurement, are located at $\theta \leq 51.13°$. The coaxial detectors are located at the larger angles.

Det.	Type	θ (deg)	x	$\frac{dx}{x}$	$\frac{N_{\gamma_{emit}}}{N_{\gamma_{escape}}}$		$\frac{d\left(\frac{N_{\gamma_{emit}}}{N_{\gamma_{escape}}}\right)}{\frac{N_{\gamma_{emit}}}{N_{\gamma_{escape}}}}$	
					Eq. 16	MCNP	Eq. 18	MCNP
^{234}U, $4^+ \rightarrow 2^+$, 99.9 keV, 12-mil 1999 target								
K	planar	6.70	0.97	0.078	1.56	1.56(1)	0.032	0.032
A,B	planar	28.73	1.10	0.080	1.65	1.66(1)	0.036	0.038
T	planar	32.40	1.14	0.081	1.68	1.68(1)	0.037	0.038
L,M	planar	33.40	1.15	0.081	1.69	1.68(1)	0.038	0.037
I,J	planar	41.80	1.29	0.084	1.78	1.81(1)	0.043	0.042
N	planar	44.70	1.35	0.085	1.83	1.81(1)	0.045	0.044
C,D	planar	51.13	1.53	0.089	1.96	1.92(1)	0.051	0.046
H	coax	58.10	1.82	0.096	2.17	2.25(1)	0.062	0.055
R,S	coax	62.19	2.06	0.102	2.36	2.48(1)	0.071	0.058
E	coax	70.40	2.87	0.125	3.04	3.03(2)	0.103	0.066
O,P	coax	72.77	3.25	0.137	3.38	3.48(2)	0.119	0.072
Q	coax	83.90	9.06	0.336	9.06	9.73(11)	0.335	0.080
F,G	coax	84.62	10.27	0.379	10.27	9.65(8)	0.378	0.084
^{234}U, $6^+ \rightarrow 4^+$, 152.7 keV, 12-mil 1999 target								
K	planar	6.70	1.34	0.078	1.81	1.83(1)	0.041	0.042
A,B	planar	28.73	1.52	0.080	1.94	1.98(1)	0.046	0.048
T	planar	32.40	1.57	0.081	1.99	2.00(1)	0.047	0.049
L,M	planar	33.40	1.59	0.081	2.00	2.03(1)	0.048	0.049
I,J	planar	41.80	1.78	0.084	2.14	2.21(1)	0.053	0.053
N	planar	44.70	1.87	0.085	2.21	2.22(2)	0.056	0.052
C,D	planar	51.13	2.12	0.089	2.41	2.38(1)	0.063	0.056
H	coax	58.10	2.51	0.096	2.74	2.85(2)	0.075	0.066
R,S	coax	62.19	2.85	0.102	3.02	3.18(2)	0.084	0.068
E	coax	70.40	3.96	0.125	4.04	4.05(3)	0.115	0.073
O,P	coax	72.77	4.49	0.137	4.54	4.62(3)	0.130	0.075
Q	coax	83.90	12.51	0.336	12.51	13.30(19)	0.336	0.080
F,G	coax	84.62	14.17	0.379	14.17	13.06(13)	0.379	0.081
^{234}U, $8^+ \rightarrow 6^+$, 201.0 keV, 12-mil 1999 target								
K	planar	6.70	0.69	0.078	1.38	1.39(1)	0.024	0.025

continued from previous page

Det.	Type	θ (deg)	x	$\frac{dx}{x}$	$\frac{N_{\gamma_{emit}}}{N_{\gamma_{escape}}}$		$\frac{d\left(\frac{N_{\gamma_{emit}}}{N_{\gamma_{escape}}}\right)}{\frac{N_{\gamma_{emit}}}{N_{\gamma_{escape}}}}$	
					Eq. 16	MCNP	Eq. 18	MCNP
A,B	planar	28.73	0.78	0.080	1.44	1.45(1)	0.027	0.028
T	planar	32.40	0.81	0.081	1.46	1.46(1)	0.028	0.028
L,M	planar	33.40	0.82	0.081	1.46	1.47(1)	0.029	0.029
I,J	planar	41.80	0.91	0.084	1.53	1.54(1)	0.032	0.032
N	planar	44.70	0.96	0.085	1.55	1.56(1)	0.034	0.031
C,D	planar	51.13	1.09	0.089	1.64	1.61(1)	0.040	0.035
H	coax	58.10	1.29	0.096	1.78	1.82(1)	0.049	0.042
R,S	coax	62.19	1.46	0.102	1.90	1.96(1)	0.057	0.046
E	coax	70.40	2.03	0.125	2.34	2.32(2)	0.087	0.055
O,P	coax	72.77	2.30	0.137	2.56	2.60(1)	0.102	0.059
Q	coax	83.90	6.41	0.336	6.42	6.79(7)	0.332	0.076
F,G	coax	84.62	7.26	0.379	7.27	6.71(5)	0.377	0.076
^{234}U, $4^+ \rightarrow 2^+$, 99.9 keV, 24-mil 1999 target								
K	planar	6.70	1.85	0.060	2.20	2.19(1)	0.040	0.043
A,B	planar	28.73	2.10	0.063	2.39	2.45(1)	0.045	0.047
T	planar	32.40	2.18	0.064	2.46	2.48(2)	0.046	0.048
L,M	planar	33.40	2.21	0.064	2.48	2.49(1)	0.047	0.048
I,J	planar	41.80	2.47	0.068	2.70	2.77(1)	0.052	0.050
N	planar	44.70	2.59	0.069	2.80	2.77(2)	0.055	0.052
C,D	planar	51.13	2.94	0.074	3.10	3.08(2)	0.062	0.055
H	coax	58.10	3.49	0.082	3.60	3.67(3)	0.073	0.059
R,S	coax	62.19	3.95	0.089	4.03	4.26(2)	0.083	0.060
E	coax	70.40	5.49	0.115	5.51	5.58(5)	0.112	0.064
O,P	coax	72.77	6.22	0.128	6.23	6.35(4)	0.126	0.064
Q	coax	83.90	17.33	0.332	17.33	18.54(29)	0.332	0.063
F,G	coax	84.62	19.65	0.375	19.65	18.18(20)	0.375	0.063
^{234}U, $6^+ \rightarrow 4^+$, 152.7 keV, 24-mil 1999 target								
K	planar	6.70	2.56	0.060	2.77	2.79(2)	0.047	0.051
A,B	planar	28.73	2.90	0.063	3.07	3.19(2)	0.052	0.054
T	planar	32.40	3.01	0.064	3.17	3.23(3)	0.054	0.057
L,M	planar	33.40	3.04	0.064	3.20	3.26(2)	0.055	0.054
I,J	planar	41.80	3.41	0.068	3.53	3.65(2)	0.060	0.059
N	planar	44.70	3.58	0.069	3.68	3.72(3)	0.062	0.060
C,D	planar	51.13	4.05	0.074	4.12	4.08(3)	0.069	0.061
H	coax	58.10	4.81	0.082	4.85	5.02(5)	0.079	0.061
R,S	coax	62.19	5.45	0.089	5.47	5.82(4)	0.087	0.064
E	coax	70.40	7.58	0.115	7.58	7.76(8)	0.115	0.068

continued from previous page

Det.	Type	θ (deg)	x	$\frac{dx}{x}$	$\frac{N_{\gamma_{emit}}}{N_{\gamma_{escape}}}$		$\frac{d\left(\frac{N_{\gamma_{emit}}}{N_{\gamma_{escape}}}\right)}{\frac{N_{\gamma_{emit}}}{N_{\gamma_{escape}}}}$	
					Eq. 16	MCNP	Eq. 18	MCNP
O,P	coax	72.77	8.58	0.128	8.58	8.69(7)	0.127	0.065
Q	coax	83.90	23.92	0.332	23.92	25.27(48)	0.332	0.066
F,G	coax	84.62	27.11	0.375	27.11	24.97(34)	0.375	0.062
^{234}U, $8^+ \rightarrow 6^+$, 201.0 keV, 24-mil 1999 target								
K	planar	6.70	1.31	0.060	1.80	1.81(1)	0.031	0.034
A,B	planar	28.73	1.49	0.063	1.92	1.97(1)	0.036	0.038
T	planar	32.40	1.54	0.064	1.96	1.97(2)	0.037	0.038
L,M	planar	33.40	1.56	0.064	1.98	1.98(1)	0.038	0.038
I,J	planar	41.80	1.75	0.068	2.12	2.14(1)	0.043	0.042
N	planar	44.70	1.83	0.069	2.18	2.20(2)	0.045	0.044
C,D	planar	51.13	2.08	0.074	2.37	2.33(1)	0.052	0.045
H	coax	58.10	2.47	0.082	2.69	2.75(2)	0.063	0.051
R,S	coax	62.19	2.79	0.089	2.98	3.13(2)	0.073	0.054
E	coax	70.40	3.88	0.115	3.97	3.95(3)	0.106	0.059
O,P	coax	72.77	4.40	0.128	4.45	4.53(3)	0.121	0.063
Q	coax	83.90	12.26	0.332	12.26	12.87(19)	0.332	0.062
F,G	coax	84.62	13.90	0.375	13.90	12.55(13)	0.375	0.066

6.4 In-beam test of attenuation correction procedure

In order to verify that the attenuation correction procedure is correct, in-beam measurements of the 157-keV $6^+ \rightarrow 4^+$ transition in ^{234}U were made with ^{235}U targets of different thicknesses. The ratio of counts observed normalized to neutron flux should be equal to the ratio of attenuation correction factors. Figure 21 shows the ratio of counts normalized by the neutron flux and attenuation correction factors. These results agree with one-sigma experimental uncertainty. The uncertainty in these ratios is dominated by the uncertainty in target areal density which propagates through to uncertainty in the attenuation correction factor.

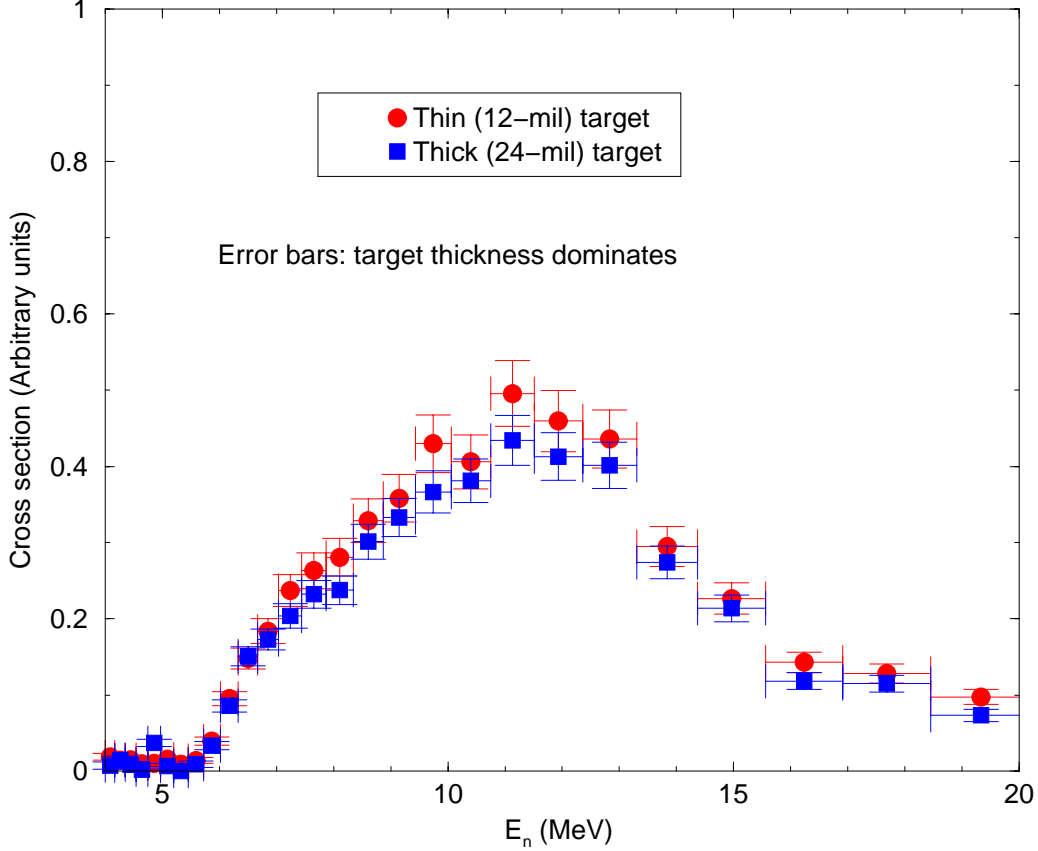## Counts scaled by attenuation correction and target thickness

Figure 21: The 157-keV $6^+ \to 4^+$ transition in ^{234}U was observed with both 12-mil and 24-mil ^{235}U targets. The ratio of counts normalized by neutron flux and the attenuation correction factor is plotted for both measurements. The error bars are dominated by uncertainties in the attenuation correction factor due to large uncertainty in the areal density of the targets.

6.5   Summary

In summary, the attenuation correction factor $\frac{N_{\gamma emit}}{N_{\gamma escape}}$ varies with target and transition energy. This ratio has been calculated with a realistic MCNP model and with an analytical model that assumes the target-detector distance is large. Both approaches give the same correction factors within Monte Carlo statistics. Because of the ease of use, the analytical model has been used to calculate $\frac{N_{\gamma emit}}{N_{\gamma escape}}$ and its relative uncertainty. This relative uncertainty is functionally dependent on $x = \mu \rho l$ as is shown in Figure 20. Larger values of x translate into larger uncertainties.

7 Internal conversion coefficients

Internal conversion coefficients for K-, L-, and M-subshells have been calculated and tabulated by Hager and Seltzer [Hag69]. Internal conversion coefficients for N-subshells have been reported by Dragoun *et al.* [Dra69]. The O- and higher subshells have not been considered here, and represent at most a 5% correction. Total internal conversion measurements in the actinides have been made for a few selected yrast transitions by Duke and Talbert [Duk68] and Ahmad *et al.* [Ahm72]. Table 18 compares experimentally determined conversion coefficients to the above-mentioned calculations. This Table also includes the Hager and Seltzer and the Dragoun calculations for internal conversion for the relevant lines in ^{238}Pu and ^{234}U.

Table 18: The first part compares experimentally measured values of α with the calculations of Hager and Seltzer [Hag69]. The second part lists the α values for the relevant transitions in ^{238}Pu and ^{234}U as interpolated from the Hager and Seltzer [Hag69] and the Dragoun [Dra69] tables.

Nucleus	E_γ (keV)	α_{expt}	α_{th}	$\alpha_{expt}/\alpha_{th}$
^{238}Pu[a]	44.1	731(73)	742	0.99(10)
^{224}Ra[b]	84.4	19.6(1.4)	20.6(9)	0.95(8)
^{228}Th[b]	57.6	158(7)	157(2)	1.01(5)
^{232}Th[b]	49.8	260(30)	321(13)	0.81(10)
^{234}U[b]	43.5	780(55)	692(8)	1.13(8)
^{236}U[b]	45.3	607(29)	612(18)	0.99(6)
^{238}U[b]	44.7	558(60)	634(26)	0.88(10)
^{240}Pu[b]	42.9	845(93)	939(9)	0.90(10)
^{238}Pu	101.9	-	14.8	-
^{238}Pu	157.4	-	2.243	-
^{238}Pu	210.0	-	0.7304	-
^{238}Pu	259.4	-	0.3463	-
^{234}U	99.8	-	13.7	-
^{234}U	152.7	-	2.192	-
^{234}U	201.0	-	0.7508	-
^{234}U	244.2	-	0.3754	-

[a] From [Ahm72]
[b] From [Duk68]

The agreement between theory and experiment is actually quite good, with only 3 of the 8 data points outside of 1σ agreement. An analysis of χ^2/ν suggests an uncertainty of about 3% in the calculations. However, the experimental uncertainties are fairly large. The papers by

Hager and Seltzer [Hag69] and Dragoun *et al.* [Dra69] do not give estimates of the reliability of their calculations. There is at least some uncertainty in the conversion coefficients given in Table 18 from not including O- and higher-subshells. Since there has been no stringent experimental test of the theoretical calculations and no error analysis on the calculations has been performed, a relatively conservative uncertainty of 6% in α, which is entirely systematical in nature, has been adopted. Note that the relevant quantity in Eq. 8 is $(1 + \alpha)$, and the uncertainty in this quantity is $\approx 3\%$ for the yrast $6^+ \rightarrow 4^+$ transitions.

8 Conclusion

The uncertainty budget at is summarized in table format for the ^{239}Pu$(n, 2n\gamma)$ and ^{235}U$(n, 2n\gamma)$ experiments at the GEANIE array located at LANSCE/WNR.

The value used for $\varepsilon_{neutron}$ is for the ^{235}U fission foil for $E_n \approx 12$ MeV. Figure 4 gives a more complete listing as a function of neutron energy. The $\frac{N_{\gamma_{emit}}}{N_{\gamma_{escape}}}$ includes the attenuation of absorbers placed on the detectors in addition to attenuation in the target and is given as an average values for representative purposes, since the uncertainty is strongly angle dependent. The $\frac{1}{\varepsilon_\gamma}$ is given for the sum of all planar detectors. The totals should be multiplied by $\frac{N_{\gamma_{obs}}}{N_{n_{obs}}}$ to give estimates of the partial cross sections. Representative values for $\frac{N_{\gamma_{obs}}}{N_{n_{obs}}}$ are discussed in [Ber00] and [You00].

Table 19: Summary of results and uncertainty budget for the ^{239}Pu$(n, 2n)$ measurement with the 10-mil target. There were 20 mils of molybdenum on the planar detectors during this experiment.

Term	$4^+ \rightarrow 2^+$	Relative standard uncertainty	$6^+ \rightarrow 4^+$	Relative standard uncertainty	$8^+ \rightarrow 6^+$	Relative standard uncertainty
$\varepsilon_{neutron}$	$\sim 1.8 \times 10^{-6}$	≈ 0.026	$\sim 1.8 \times 10^{-6}$	≈ 0.026	$\sim 1.8 \times 10^{-6}$	≈ 0.026
$\frac{1}{\varepsilon_\gamma}$	27.23	0.031	36.23	0.031	51.05	0.031
$\frac{N_{\gamma_{emit}}}{N_{\gamma_{escape}}}$	2.37	0.042	1.94	0.039	1.37	0.034
$1 + \alpha$	15.8	0.056	3.24	0.041	1.73	0.025
$\frac{A}{\rho l N_A} \left(\frac{barns}{atom}\right)$	952.21	0.019	952.21	0.019	952.21	0.019
Totals	1.75	0.083	0.390	0.072	0.207	0.061

Table 20: Summary of results and uncertainty budget for the ^{239}Pu$(n, 2n)$ measurement with the 20-mil target. There were 20 mils of molybdenum on the planar detectors during this experiment.

Term	$4^+ \rightarrow 2^+$	Relative standard uncertainty	$6^+ \rightarrow 4^+$	Relative standard uncertainty	$8^+ \rightarrow 6^+$	Relative standard uncertainty
$\varepsilon_{neutron}$	$\sim 1.8 \times 10^{-6}$	≈ 0.026	$\sim 1.8 \times 10^{-6}$	≈ 0.026	$\sim 1.8 \times 10^{-6}$	≈ 0.026
$\frac{1}{\varepsilon_\gamma}$	27.23	0.031	36.23	0.031	51.05	0.031
$\frac{N_{\gamma_{emit}}}{N_{\gamma_{escape}}}$	3.25	0.048	2.85	0.045	1.72	0.038
$1 + \alpha$	15.8	0.056	3.24	0.041	1.73	0.025
$\frac{A}{\rho l N_A} \left(\frac{barns}{atom}\right)$	517.48	0.007	517.48	0.007	517.48	0.007
Totals	1.30	0.084	0.312	0.073	0.141	0.061

Table 21: Summary of results and uncertainty budget for the ^{235}U$(n, 2n)$ measurement with the 1998 12-mil target. There were no absorbers on the detectors during this experiment.

Term	$4^+ \to 2^+$	Relative standard uncertainty	$6^+ \to 4^+$	Relative standard uncertainty	$8^+ \to 6^+$	Relative standard uncertainty
$\varepsilon_{neutron}$	$\sim 1.8 \times 10^{-6}$	≈ 0.026	$\sim 1.8 \times 10^{-6}$	≈ 0.026	$\sim 1.8 \times 10^{-6}$	≈ 0.026
$\frac{1}{\varepsilon_\gamma}$	27.12	0.031	35.13	0.031	48.57	0.031
$\frac{N_{\gamma_{emit}}}{N_{\gamma_{escape}}}$	1.57	0.050	1.88	0.059	1.35	0.044
$1 + \alpha$	14.7	0.056	3.19	0.041	1.75	0.026
$\frac{A}{\rho l N_A} \left(\frac{barns}{atom} \right)$	744.58	0.071	744.58	0.071	744.58	0.071
Totals	0.839	0.111	0.282	0.109	0.154	0.096

Table 22: Summary of results and uncertainty budget for the ^{235}U$(n, 2n)$ measurement with the 1998 24-mil target. There were no absorbers on the detectors during this experiment.

Term	$4^+ \to 2^+$	Relative standard uncertainty	$6^+ \to 4^+$	Relative standard uncertainty	$8^+ \to 6^+$	Relative standard uncertainty
$\varepsilon_{neutron}$	$\sim 1.8 \times 10^{-6}$	≈ 0.026	$\sim 1.8 \times 10^{-6}$	≈ 0.026	$\sim 1.8 \times 10^{-6}$	≈ 0.026
$\frac{1}{\varepsilon_\gamma}$	27.12	0.031	35.13	0.031	48.57	0.031
$\frac{N_{\gamma_{emit}}}{N_{\gamma_{escape}}}$	2.24	0.056	2.90	0.064	1.80	0.050
$1 + \alpha$	14.7	0.056	3.19	0.041	1.75	0.026
$\frac{A}{\rho l N_A} \left(\frac{barns}{atom} \right)$	389.33	0.050	389.33	0.050	389.33	0.050
Totals	0.626	0.102	0.228	0.100	0.107	0.086

Table 23: Summary of results and uncertainty budget for the ^{235}U$(n, 2n)$ measurement with the 1999 12-mil target. There were 20 mils of molybdenum on the planar detectors during this experiment.

Term	$4^+ \rightarrow 2^+$	Relative standard uncertainty	$6^+ \rightarrow 4^+$	Relative standard uncertainty	$8^+ \rightarrow 6^+$	Relative standard uncertainty
$\varepsilon_{neutron}$	$\sim 1.8 \times 10^{-6}$	≈ 0.026	$\sim 1.8 \times 10^{-6}$	≈ 0.026	$\sim 1.8 \times 10^{-6}$	≈ 0.026
$\frac{1}{\varepsilon_\gamma}$	27.12	0.031	35.13	0.031	48.57	0.031
$\frac{N_{\gamma_{emit}}}{N_{\gamma_{escape}}}$	2.49	0.043	2.08	0.039	1.43	0.034
$1 + \alpha$	14.7	0.056	3.19	0.041	1.75	0.026
$\frac{A}{\rho l N_A}$ $\left(\frac{barns}{atom}\right)$	868.18	0.006	868.18	0.006	868.18	0.006
Totals	1.55	0.082	0.364	0.070	0.190	0.059

9   References

References

[Ahm72]   I. Ahmad, *et al.*, Nucl. Phys. **A186**, 620 (1980).

[Alice]   M. Blann and H. K. Vonach, Phys. Rev. **28**, 1475 (1983).

[Ber99]   L. Bernstein, private communication (1999).

[Ber00]   L. A. Bernstein *et al.*, "Measurement of several ^{239}Pu(n,xn) partial γ-ray cross sections for $x \leq 3$ using GEANIE at LANSCE/WNR," (2000).

[Bre99]   J. Bremser and M. Gross, private communication (1999).

[Car74]   G. W. Carlson, Nucl. Inst. Meth. **119**, 97 (1974).

[Con70]   A. L. Conner *et al.*, Phys. Rev. **A1**, 539 (1970).

[Con99]   C. Conrado, private communication (1999).

[Cro95]   B. Crowell, M. P. Carpenter, R. G. Henry, R. V. F. Janssens, T. L. Khoo, T. Lauritsen, and D. Nisius, Nucl. Inst. and Meth. in Phys. Res. **A355** 575 (1995).

[Dra69]   O. Dragoun, H. C. Pauli, and F. Schmutzler, Nucl. Data Tables **A6**, 235 (1969).

[Duk68]   C. L. Duke and W. L. Talbert, Jr., Phys. Rev. **173**, 172 (1968).

[Gal99]   G. Gallegos, private communication (1999).

[Hag69]   R. S. Hager and E. C. Seltzer, Nucl. Data Tables **A6**, 1 (1969).

[Hel98]   R. G. Helmer, private communication (1998). The quoted values were taken from the DDEP and IAEA-TECDOC-619 evaluations.

[Kno79]   G. F. Knoll, *Radiation Detection and Measurement,* John Wiley and Sons, New York, Chapter 3 (1979).

[McC67]   J. H. McCrary *et al.*, Phys. Rev. **153**, 307 (1967).

[Miy86]   J. Miyahara *et al.*, Nucl. Inst. and Meth. in Phys. Res. **A246** 572 (1986).

[Nel99]   R. Nelson, private communication (1999).

[Nel00]   R. Nelson, private communication (1999). Calculation done with code COLIM.FOR written by Steve Wender.

[Nii94]   N. Niimura *et al.*, Nucl. Inst. and Meth. in Phys. Res. **A349** 521 (1994).

[Sal88]   E. B. Saloman, J. H. Hubbell, and J. H. Scofield, At. Data and Nucl. Data Tables **38**, 1 (1988).

[Sto70]   E. Storm and H. I. Israel, Nucl. Data Tables **A7**, 565 (1970).

[Sub]   C. Sublette, *Nuclear Weapons Frequently Asked Questions*, as found at http://centurychina.com/wiihist/japarms/pu239.html.

[Tay94]   B. N. Taylor and C. F. Kuyatt, *Guidelines for Evaluating and Expressing the Uncertainty of NIST Measurement Results*, NIST Technical Note 1297, (1994).

[Vei73]   W. J. Veigele, At. Data **5**, 52 (1973).

[Wen93]   S. A. Wender *et al.*, Nucl. Inst. Meth. **A336**, 226 (1993); S. A. Wender *et al.*, LAUR 90-3399.

[XCOM]   XCOM program found at http://physics.nist.gov/PhysRefData/Xcom/Text/XCOM.html.

[You98]   W. Younes *et al.*, "Measurement of the ^{235}U$(n, 2n)$ cross section using GEANIE at LANSCE/WNR: progress report on the 1997 data and analysis techniques," UCRL-ID-132627, (1998).

[You98b]   W. Younes, private communication (1998).

[You99]   W. Younes, private communication (1999).

[You99b]   W. Younes, private communication (1999).

[You00]   W. Younes *et al.*, "The ^{235}U(n,2nγ) Yrast Partial Gamma-Ray Cros Sections: A Report on the 1998 and 1999 GEANIE Data and Analysis Techniques," (2000).

A Location and description of relevant files and codes

In this appendix, the location and description of important production files for calculating the array efficiency is discussed. The majority of the sorting, analysis, and coding was done on dollar.llnl.gov. The only exception is that the MCNP calculations were done on the Compass cluster and are described in Appendix B.

Figure 22 shows the directory structure for production files. The root directory is */home/mcnabb/efficiency*. The main production code is EFFICIENCY.PL, which is located in the root directory. The *pteff, extended,* and *mutables* subdirectories contain the supporting data files that efficiency.pl uses for calculating an in-beam efficiency.
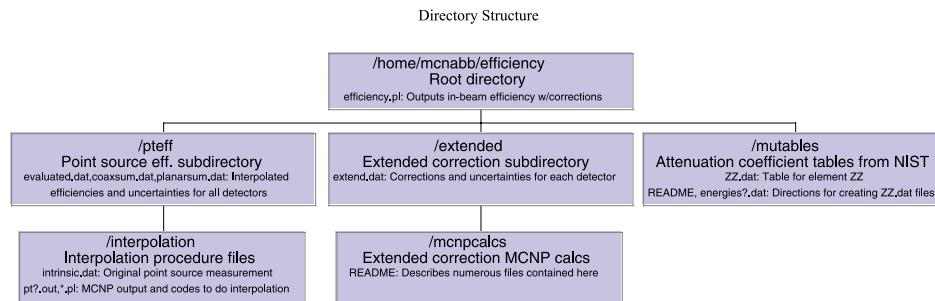

Figure 22: Directory structure for important production files on dollar.llnl.gov.

An example of how to use EFFICIENCY.PL for an experiment is shown here for a 10-mil ^{239}Pu target:

```
~ % mkdir pu10mil
~ % cd pu10mil
~/pu10mil % /home/mcnabb/efficiency/efficiency.pl
Z of target: 94
Areal density in g/cm^2: 0.4305
Relative uncertainty in areal density: 0.019
Are the absorbers on the detectors or not (Y/N)? Y
~/pu10mil % ls
alldetectors.out    coaxsum.out         planarsum.out
~/pu10mil %
```

The point source absolute peak efficiencies used by EFFICIENCY.PL are found in the subdirectory *pteff*. The values for each detector are listed in steps of 10 keV inside the file *evaluated.dat*. The relative uncertainties given in the third column of the file represent the statistical measurement uncertainty and the uncertainty of the interpolation procedure. The uncertainty in source strength is added in separately inside EFFICIENCY.PL. The other files *coaxsum.dat* and *planarsum.dat* are included here for experimenters who are just interested in relative efficiencies. The files and codes used to do the interpolation to every 10 keV is found in the

subdirectory *pteff/interpolation.* There are three codes in this directory: *interpolation.pl, get-calcs.pl,* and *getpts.pl.* The code *interpolation.pl* reads the measured efficiencies in *intrinsic.dat* and the calculated efficiencies in *mcnp_calc-pt.dat* and *mcnp_calc-all.dat* and does the required interpolation. The measured point source peak efficiency values and the method by which they were obtained are described in Section 4.

The extended corrections and relative uncertainties are listed in the file *extended/extend.dat.* The myriad of calculations done to obtain these numbers are found in the subdirectory *extended/mcnpcalcs.*

The file required to do the attenuation corrections are contained in the subdirectory *mutables.* The attenuation coefficients have been downloaded from the NIST website http://physics.nist.gov/PhysRefData/Xcom/html/xcom1.html. A description of the procedure can be found in the file *mutables/README.* The attenuation coefficients for iron, molybdenum, tin, tantalum, uranium, and plutonium have already been downloaded and stored in the files em ZZ.dat whare *ZZ* is the atomic number. The molybdenum, tin, and tantalum values are used to correct for absorbers on the detectors. The absorbers, if present, are assumed to be 20 mils of molybdenum on the planar detectors and 10 mils of tin plus 10 mils of tantalum on the coaxial detectors. Other configurations will require a modification of EFFICIENCY.PL.

B MCNP model of GEANIE array

MCNP has been used to (1) verify that measurements make sense, (2) interpolate between measured values, and (3) calculate the correction for beam geometry and its uncertainty. The MCNP input files reside on the Compass cluster at LLNL under /g/g19/mcnabb/array/mcnp. This Appendix includes a description of what is contained in this directory tree, as well as a hard copy listing of of an MCNP input file.

Here is an MCNP input file which was used as part of the interpolation procedure. This geometry includes the absorbers, but they were voided out. The MCNP input file used to do the correction for beam geometry was deemed too long for hard copy since the beam spot description takes approximately 250 pages to list. Please see the discussion above to find the input file on the Compass cluster.

```
c---geanie array  MCNP file     8/1/98
c       Detector setup for August 1998
c       Target:  239Pu
c       Dectectors with Be windows, except Q which is Al
c       No absorbers
c       Be windows at a mean of 14.37 cm
c
c
c
c       DETECTOR A
c
11     0 -12 -13 15 imp:p=1 trcl=1 fill=1     $Detector cell
12     32 -5.32 10 -11 imp:p=1 u=1            $leps detector crystal
13     4 -1.85 -14 imp:p=1 u=1                $Be window
14     0 #12 #13 imp:p=1 u=1                  $vacuum inside detector
15     0 -16 815 -19 imp:p=1 trcl=1 fill=2    $collimator cell
16     82 -11.4 18 17 imp:p=1 u=2             $collimator
17     2 -0.0012929 -18 17 imp:p=1 u=2        $inside collimator
18     0 -17 imp:p=1 u=2               $Mo absorber
c
c       DETECTOR B
c
21     0 -22 -23 25 imp:p=1 trcl=2 fill=3     $Detector cell
22     32 -5.32 20 -21 imp:p=1 u=3            $leps detector crystal
23     4 -1.85 -24 imp:p=1 u=3                $Be window
24     0 #22 #23 imp:p=1 u=3                  $vacuum inside detector
25     0 -26 825 -29 imp:p=1 trcl=2 fill=4    $collimator cell
26     82 -11.4 28 27 imp:p=1 u=4             $collimator
27     2 -0.0012929 -28 27 imp:p=1 u=4        $inside collimator
28     0 -27 imp:p=1 u=4               $Mo absorber
c
```

```
c      DETECTOR C
c
31    0 -32 -33 35 imp:p=1 trcl=3 fill=5      $Detector cell
32    32 -5.32 30 -31 imp:p=1 u=5             $leps detector crystal
33    4 -1.85 -34 imp:p=1 u=5                 $Be window
34    0 #32 #33 imp:p=1 u=5                   $vacuum inside detector
35    0 -36 835 -39 imp:p=1 trcl=3 fill=6     $collimator cell
36    82 -11.4 38 37 imp:p=1 u=6              $collimator
37    2 -0.0012929 -38 37 imp:p=1 u=6         $inside collimator
38    0 -37 imp:p=1 u=6              $Mo absorber
c
c      DETECTOR D
c
41    0 -42 -43 45 imp:p=1 trcl=4 fill=7      $Detector cell
42    32 -5.32 40 -41 imp:p=1 u=7             $leps detector crystal
43    4 -1.85 -44 imp:p=1 u=7                 $Be window
44    0 #42 #43 imp:p=1 u=7                   $vacuum inside detector
45    0 -46 845 -49 imp:p=1 trcl=4 fill=8     $collimator cell
46    82 -11.4 48 47 imp:p=1 u=8              $collimator
47    2 -0.0012929 -48 47 imp:p=1 u=8         $inside collimator
48    0 -47 imp:p=1 u=8              $Mo absorber
c
c      DETECTOR E
c
51    0 -52 -53 55 imp:p=1 trcl=5 fill=9      $Detector cell
52    32 -5.32 50 -51 #(-851 852) #(853) imp:p=1 u=9 $coax crystal
53    4 -1.85 -54 imp:p=1 u=9                 $Be window
54    0 #52 #53 imp:p=1 u=9                   $vacuum inside detector
55    0 -56 856 -59 imp:p=1 trcl=5 fill=10    $collimator cell
56    82 -11.4 58 57 imp:p=1 u=10             $collimator
57    2 -0.0012929 -58 57 imp:p=1 u=10        $inside collimator
58    0 -57 855 imp:p=1 u=10        $Ta absorber
59    0 -855  imp:p=1 u=10          $Sn absorber
c
c      DETECTOR F
c
61    0 -62 -63 65 imp:p=1 trcl=6 fill=11     $Detector cell
62    32 -5.32 60 -61 #(-861 862) #(863) imp:p=1 u=11 $coax crystal
63    4 -1.85 -64 imp:p=1 u=11               $Be window
64    0 #62 #63 imp:p=1 u=11                  $vacuum inside detector
65    0 -66 866 -69 imp:p=1 trcl=6 fill=12    $collimator cell
66    82 -11.4 68 67 imp:p=1 u=12             $collimator
67    2 -0.0012929 -68 67 imp:p=1 u=12        $inside collimator
```

```
68    0 -67 865 imp:p=1 u=12              $Ta absorber
69    0 -865 imp:p=1 u=12                $Sn absorber
c
c     DETECTOR G
c
71    0 -72 -73 75 imp:p=1 trcl=7 fill=13    $Detector cell
72    32 -5.32 70 -71 #(-871 872) #(873) imp:p=1 u=13 $coax crystal
73    4 -1.85 -74 imp:p=1 u=13                $Be window
74    0 #72 #73 imp:p=1 u=13                  $vacuum inside detector
75    0 -76 876 -79 imp:p=1 trcl=7 fill=14    $collimator cell
76    82 -11.4 78 77 imp:p=1 u=14             $collimator
77    2 -0.0012929 -78 77 imp:p=1 u=14        $inside collimator
78    0 -77 875 imp:p=1 u=14          $Ta absorber
79    0 -875 imp:p=1 u=14             $Sn absorber
c
c     DETECTOR H
c
81    0 -82 -83 85 imp:p=1 trcl=8 fill=15    $Detector cell
82    32 -5.32 80 -81 #(-881 882) #(883) imp:p=1 u=15 $coax crystal
83    4 -1.85 -84 imp:p=1 u=15                $Be window
84    0 #82 #83 imp:p=1 u=15                  $vacuum inside detector
85    0 -86 886 -89 imp:p=1 trcl=8 fill=16    $collimator cell
86    82 -11.4 88 87 imp:p=1 u=16             $collimator
87    2 -0.0012929 -88 87 imp:p=1 u=16        $inside collimator
88    0 -87 885 imp:p=1 u=16          $Ta absorber
89    0 -885 imp:p=1 u=16             $Sn absorber
c
c     DETECTOR I
c
91    0 -92 -93 95 imp:p=1 trcl=9 fill=17    $Detector cell
92    32 -5.32 90 -91 imp:p=1 u=17           $leps detector crystal
93    4 -1.85 -94 imp:p=1 u=17               $Be window
94    0 #92 #93 imp:p=1 u=17                 $vacuum inside detector
95    0 -96 895 -99 imp:p=1 trcl=9 fill=18   $collimator cell
96    82 -11.4 98 97 imp:p=1 u=18            $collimator
97    2 -0.0012929 -98 97 imp:p=1 u=18       $inside collimator
98    0 -97 imp:p=1 u=18              $Mo absorber
c
c     DETECTOR J
c
101    0 -102 -103 105 imp:p=1 trcl=10 fill=19 $Detector cell
102    32 -5.32 100 -101 imp:p=1 u=19          $leps detector crystal
103    4 -1.85 -104 imp:p=1 u=19               $Be window
```

```
104    0 #102 #103 imp:p=1 u=19                $vacuum inside detector
105    0 -106 905 -109 imp:p=1 trcl=10 fill=20 $collimator cell
106    82 -11.4 108 107 imp:p=1 u=20           $collimator
107    2 -0.0012929 -108 107 imp:p=1 u=20      $inside collimator
108    0 -107 imp:p=1 u=20            $Mo absorber
c
c    DETECTOR K
c
111    0 -112 -113 115 imp:p=1 trcl=11 fill=21 $Detector cell
112    32 -5.32 110 -111 imp:p=1 u=21          $leps detector crystal
113    4 -1.85 -114 imp:p=1 u=21               $Be window
114    0 #112 #113 imp:p=1 u=21                $vacuum inside detector
115    0 -116 915 -119 imp:p=1 trcl=11 fill=22 $collimator cell
116    82 -11.4 118 117 imp:p=1 u=22           $collimator
117    2 -0.0012929 -118 117 imp:p=1 u=22      $inside collimator
118    0 -117 imp:p=1 u=22            $Mo absorber
c
c    DETECTOR L
c
121    0 -122 -123 125 imp:p=1 trcl=12 fill=23 $Detector cell
122    32 -5.32 120 -121 imp:p=1 u=23          $leps detector crystal
123    4 -1.85 -124 imp:p=1 u=23               $Be window
124    0 #122 #123 imp:p=1 u=23                $vacuum inside detector
125    0 -126 925 -129 imp:p=1 trcl=12 fill=24 $collimator cell
126    82 -11.4 128 127 imp:p=1 u=24           $collimator
127    2 -0.0012929 -128 127 imp:p=1 u=24      $inside collimator
128    0 -127 imp:p=1 u=24            $Mo absorber
c
c    DETECTOR M
c
131    0 -132 -133 135 imp:p=1 trcl=13 fill=25 $Detector cell
132    32 -5.32 130 -131 imp:p=1 u=25          $leps detector crystal
133    4 -1.85 -134 imp:p=1 u=25               $Be window
134    0 #132 #133 imp:p=1 u=25                $vacuum inside detector
135    0 -136 935 -139 imp:p=1 trcl=13 fill=26 $collimator cell
136    82 -11.4 138 137 imp:p=1 u=26           $collimator
137    2 -0.0012929 -138 137 imp:p=1 u=26      $inside collimator
138    0 -137 imp:p=1 u=26            $Mo absorber
c
c    DETECTOR N
c
141    0 -142 -143 145 imp:p=1 trcl=14 fill=27 $Detector cell
142    32 -5.32 140 -141 imp:p=1 u=27          $leps detector crystal
```

```
143    4 -1.85 -144 imp:p=1 u=27                    $Be window
144    0 #142 #143 imp:p=1 u=27                     $vacuum inside detector
145    0 -146 945 -149 imp:p=1 trcl=14 fill=28 $collimator cell
146    82 -11.4 148 147 imp:p=1 u=28               $collimator
147    2 -0.0012929 -148 147 imp:p=1 u=28          $inside collimator
148    0 -147 imp:p=1 u=28                         $Mo absorber
c
c      DETECTOR O
c
151    0 -152 -153 155 imp:p=1 trcl=15 fill=29 $Detector cell
152    32 -5.32 150 -151 #(-951 952) #(953) imp:p=1 u=29 $coax crystal
153    4 -1.85 -154 imp:p=1 u=29                    $Be window
154    0 #152 #153 imp:p=1 u=29                     $vacuum inside detector
155    0 -156 956 -159 imp:p=1 trcl=15 fill=30 $collimator cell
156    82 -11.4 158 157 imp:p=1 u=30               $collimator
157    2 -0.0012929 -158 157 imp:p=1 u=30          $inside collimator
158    0 -157 955 imp:p=1 u=30        $Ta absorber
159    0 -955 imp:p=1 u=30            $Sn absorber
c
c      DETECTOR P
c
161    0 -162 -163 165 imp:p=1 trcl=16 fill=31 $Detector cell
162    32 -5.32 160 -161 #(-961 962) #(963) imp:p=1 u=31 $coax crystal
163    4 -1.85 -164 imp:p=1 u=31                    $Be window
164    0 #162 #163 imp:p=1 u=31                     $vacuum inside detector
165    0 -166 966 -169 imp:p=1 trcl=16 fill=32 $collimator cell
166    82 -11.4 168 167 imp:p=1 u=32               $collimator
167    2 -0.0012929 -168 167 imp:p=1 u=32          $inside collimator
168    0 -167 965 imp:p=1 u=32        $Ta absorber
169    0 -965 imp:p=1 u=32            $Sn absorber
c
c      DETECTOR Q
c
171    0 -172 -173 175 imp:p=1 trcl=17 fill=33 $Detector cell
172    32 -5.32 170 -171 #(-971 972) #(973) imp:p=1 u=33 $coax crystal
173    13 -2.6989 -174 imp:p=1 u=33               $Al window
174    0 #172 #173 imp:p=1 u=33                     $vacuum inside detector
175    0 -176 976 -179 imp:p=1 trcl=17 fill=34 $collimator cell
176    82 -11.4 178 177 imp:p=1 u=34               $collimator
177    2 -0.0012929 -178 177 imp:p=1 u=34          $inside collimator
178    0 -177 975 imp:p=1 u=34        $Ta absorber
179    0 -975 imp:p=1 u=34            $Sn absorber
c
```

```
c     DETECTOR R
c
181    0 -182 -183 185 imp:p=1 trcl=18 fill=35 $Detector cell
182    32 -5.32 180 -181 #(-981 982) #(983) imp:p=1 u=35 $coax crystal
183    4 -1.85 -184 imp:p=1 u=35              $Be window
184    0 #182 #183 imp:p=1 u=35               $vacuum inside detector
185    0 -186 986 -189 imp:p=1 trcl=18 fill=36 $collimator cell
186    82 -11.4 188 187 imp:p=1 u=36          $collimator
187    2 -0.0012929 -188 187 imp:p=1 u=36     $inside collimator
188    0 -187 985 imp:p=1 u=36        $Ta absorber
189    0 -985 imp:p=1 u=36            $Sn absorber
c
c     DETECTOR S
c
191    0 -192 -193 195 imp:p=1 trcl=19 fill=37 $Detector cell
192    32 -5.32 190 -191 #(-991 992) #(993) imp:p=1 u=37 $coax crystal
193    4 -1.85 -194 imp:p=1 u=37              $Be window
194    0 #192 #193 imp:p=1 u=37               $vacuum inside detector
195    0 -196 996 -199 imp:p=1 trcl=19 fill=38 $collimator cell
196    82 -11.4 198 197 imp:p=1 u=38          $collimator
197    2 -0.0012929 -198 197 imp:p=1 u=38     $inside collimator
198    0 -197 995 imp:p=1 u=38        $Ta absorber
199    0 -995 imp:p=1 u=38            $Sn absorber
c
c     DETECTOR T
c
201    0 -202 -203 205 imp:p=1 trcl=20 fill=39 $Detector cell
202    32 -5.32 200 -201 imp:p=1 u=39         $leps detector crystal
203    4 -1.85 -204 imp:p=1 u=39              $Be window
204    0 #202 #203 imp:p=1 u=39               $vacuum inside detector
205    0 -206 705 -209 imp:p=1 trcl=20 fill=40 $collimator cell
206    82 -11.4 208 207 imp:p=1 u=40          $collimator
207    2 -0.0012929 -208 207 imp:p=1 u=40     $inside collimator
208    0 -207 imp:p=1 u=40           $Mo absorber
c
c     Point source
c
5100   2 -0.0012929 -5101 -5001 5002  imp:p=1  $Point source disk
c
1  2  -0.0032 -1 2 -3 -4 #41 #45 #51 #55 #71 #75
             #(-5101 -5001 5002) #85 imp:p=1 $upstream right lower
2  2  -0.0032 -1 2 -3 4 #31 #35 #51 #55 #61 #65
             #(-5101 -5001 5002) #85 imp:p=1 $upstream right upper
```

```
3   2  -0.0032 -1 -2 -3 -4 #21 #25 #201 #205 #191 #195
                #(-5101 -5001 5002) #175 imp:p=1 $upstream left lower
4   2  -0.0032 -1 -2 -3 4 #11 #15 #201 #205 #181 #185
                #(-5101 -5001 5002) #175 imp:p=1 $upstream left upper
5   2  -0.0032 -1 2 3 -4 #81 #85 #101 #105 #111 #115 #131 #135 #71
                #(-5101 -5001 5002) #75 imp:p=1 $downstream right lower
6   2  -0.0032 -1 2 3 4 #81 #85 #91 #95 #111 #115 #121 #125 #61
                #(-5101 -5001 5002) #65 imp:p=1 $downstream right upper
7   2  -0.0032 -1 -2 3 -4 #131 #135 #141 #145 #161 #165 #171 #175 #191
                #(-5101 -5001 5002) #195 imp:p=1 $downstream left lower
8   2  -0.0032 -1 -2 3 4 #121 #125 #141 #145 #151 #155 #171 #175 #181
                #(-5101 -5001 5002) #185 imp:p=1 $downstream left upper
10  0   1 imp:p=0   $The outside


c
c    DETECTOR A
c
c    detector crystal
10    py 14.955
11    cy 2.31
12    py 16.455
c    Cryostat surface
13    cy 2.7
c    Be window
14    py 14.455
15    py 14.415
c    Pb collimator
16    py 9.49
17    py 6.92
18    ky 0.50 0.021
19    ky 2.43 0.1552
815   py 6.8692
c
c    DETECTOR B
c
c    detector crystal
20    py 14.992
21    cy 2.42
22    py 16.882
c    Cryostat surface
23    cy 2.7
c    Be window
24    py 14.492
```

```
25      py 14.442
c       Pb collimator
26       py 9.48
27       py 6.91
28       ky 0.49 0.021
29       ky 2.42 0.1552
825      py 6.8592
c
c       DETECTOR C
c
c       detector crystal
30       py 14.929
31       cy 2.36
32       py 16.719
c       Cryostat surface
33       cy 2.7
c       Be window
34       py 14.429
35       py 14.379
c       Pb collimator
36       py 9.37
37       py 6.80
38       ky 0.38 0.021
39       ky 2.31 0.1552
835      py 6.7492
c
c       DETECTOR D
c
c       detector crystal
40       py 14.868
41       cy 2.33
42       py 16.708
c       Cryostat surface
43       cy 2.7
c       Be window
44       py 14.368
45       py 14.318
c       Pb collimator
46       py 9.48
47       py 6.91
48       ky 0.49 0.021
49       ky 2.42 0.1552
845      py 6.8592
```

```
c
c     DETECTOR E
c
c     detector core
851   ky -0.113 0.00121946
852   py 15.287
c     detector crystal
853   ky 12.562 1
50    py 14.587
51    cy 2.545
52    py 20.047
c     Cryostat surface
53    cy 2.7
c     Be window
54    py 14.287
55    py 14.237
c     Pb collimator
56    py 9.35
57    py 6.78
58    ky 0.36 0.021
59    ky 2.29 0.1552
855   py 6.7546
856   py 6.7292
c
c     DETECTOR F
c
c     detector core
861   ky -0.062 0.00121946
862   py 15.338
c     detector crystal
863   ky 12.718 1
60    py 14.638
61    cy 2.44
62    py 19.738
c     Cryostat surface
63    cy 2.7
c     Be window
64    py 14.338
65    py 14.288
c     Pb collimator
66    py 9.78
67    py 7.21
68    ky 0.79 0.021
```

```
69     ky 2.72 0.1552
865    py 7.1846
866    py 7.1592
c
c      DETECTOR G
c
c      detector core
871    ky -0.008 0.00121946
872    py 15.392
c      detector crystal
873    ky 12.752 1
70     py 14.742
71     cy 2.51
72     py 19.492
c      Cryostat surface
73     cy 2.7
c      Be window
74     py 14.442
75     py 14.392
c      Pb collimator
76     py 9.92
77     py 7.35
78     ky 0.93 0.021
79     ky 2.86 0.1552
875    py 7.3246
876    py 7.2992
c
c      DETECTOR H
c
c      detector core
881    ky 0.667 0.00121946
882    py 16.067
c      detector crystal
883    ky 13.242 1
80     py 15.267
81     cy 2.545
82     py 20.957
c      Cryostat surface
83     cy 2.7
c      Be window
84     py 14.967
85     py 14.917
c      Pb collimator
```

```
86      py 10.08
87      py 7.51
88      ky 1.09 0.021
89      ky 3.02 0.1552
885     py 7.4846
886     py 7.4592
c
c       DETECTOR I
c
c       detector crystal
90       py 15.005
91       cy 2.46
92       py 16.805
c       Cryostat surface
93       cy 2.7
c       Be window
94       py 14.505
95       py 14.455
c       Pb collimator
96       py 9.54
97       py 6.97
98       ky 0.55 0.021
99       ky 2.48 0.1552
895      py 6.9192
c
c       DETECTOR J
c
c       detector crystal
100      py 14.985
101      cy 2.41
102      py 16.685
c       Cryostat surface
103      cy 2.7
c       Be window
104      py 14.485
105      py 14.435
c       Pb collimator
106      py 9.41
107      py 6.84
108      ky 0.42 0.021
109      ky 2.35 0.1552
905      py 6.7892
c
```

```
c     DETECTOR K
c
c     detector crystal
110    py 14.858
111    cy 2.55
112    py 16.558
c     Cryostat surface
113    cy 2.7
c     Be window
114    py 14.358
115    py 14.308
c     Pb collimator
116    py 9.42
117    py 6.85
118    ky 0.43 0.021
119    ky 2.36 0.1552
915    py 6.7992
c
c     DETECTOR L
c
c     detector crystal
120    py 14.929
121    cy 2.44
122    py 16.579
c     Cryostat surface
123    cy 2.7
c     Be window
124    py 14.429
125    py 14.379
c     Pb collimator
126    py 9.55
127    py 6.98
128    ky 0.56 0.021
129    ky 2.49 0.1552
925    py 6.9292
c
c     DETECTOR M
c
c     detector crystal
130    py 15.323
131    cy 2.40
132    py 17.223
c     Cryostat surface
```

```
133     cy 2.7
c    Be window
134     py 14.814
135     py 14.764
c    Pb collimator
136     py 9.97
137     py 7.40
138     ky 0.98 0.021
139     ky 2.91 0.1552
935     py 7.3492
c
c    DETECTOR N
c
c    detector crystal
140     py 14.942
141     cy 2.44
142     py 16.342
c    Cryostat surface
143     cy 2.7
c    Be window
144     py 14.442
145     py 14.392
c    Pb collimator
146     py 9.56
147     py 6.99
148     ky 0.57 0.021
149     ky 2.50 0.1552
945     py 6.9392
c
c    DETECTOR O
c
c    detector core
951     ky 0.025 0.00121946
952     py 15.425
c    detector crystal
953     ky 12.767 1
150     py 14.742
151     cy 2.495
152     py 20.162
c    Cryostat surface
153     cy 2.7
c    Be window
154     py 14.442
```

```
155     py 14.392
c    Pb collimator
156     py 9.51
157     py 6.94
158     ky 0.52 0.021
159     ky 2.45 0.1552
955     py 6.9146
956     py 6.8892
c
c    DETECTOR P
c
c
c    detector core
961     ky -0.371 0.00121946
962     py 15.029
c    detector crystal
963     ky 12.381 1
160     py 14.296
161     cy 2.435
162     py 20.196
c    Cryostat surface
163     cy 2.7
c    Be window
164     py 13.896
165     py 13.846
c    Pb collimator
166     py 8.79
167     py 6.22
168     ky -0.20 0.021
169     ky 1.73 0.1552
965     py 6.1946
966     py 6.1692
c
c    DETECTOR Q  *** Special note: Aluminum endcap ***
c
c    detector core
971     ky 0.125 0.00121946
972     py 15.525
c    detector crystal
973     ky 12.762 1
170     py 14.792
171     cy 2.55
172     py 20.082
```

```
c     Cryostat surface
173    cy 2.7
c     Al window
174    py 14.492
175    py 14.442
c     Pb collimator
176    py 9.67
177    py 7.10
178    ky 0.68 0.021
179    ky 2.61 0.1552
975    py 7.0746
976    py 7.0492
c
c     DETECTOR R
c
c     detector core
981    ky -0.157 0.00121946
982    py 15.243
c     detector crystal
983    ky 12.521 1
180    py 14.526
181    cy 2.525
182    py 20.096
c     Cryostat surface
183    cy 2.7
c     Be window
184    py 14.226
185    py 14.176
c     Pb collimator
186    py 9.44
187    py 6.87
188    ky 0.45 0.021
189    ky 2.38 0.1552
985    py 6.8446
986    py 6.8192
c
c     DETECTOR S
c
c     detector core
991    ky 0.041 0.00121946
992    py 15.441
c     detector crystal
993    ky 12.713 1
```

```
190     py 14.658
191     cy 2.465
192     py 19.928
c    Cryostat surface
193     cy 2.7
c    Be window
194     py 14.358
195     py 14.308
c    Pb collimator
196     py 9.36
197     py 6.79
198     ky 0.37 0.021
199     ky 2.30 0.1552
995     py 6.7646
996     py 6.7392
c
c    DETECTOR T
c
c    detector crystal
200     py 14.711
201     cy 2.35
202     py 16.661
c    Cryostat surface
203     cy 2.7
c    Be window
204     py 14.211
205     py 14.161
c    Pb collimator
206     py 9.33
207     py 6.76
208     ky 0.34 0.021
209     ky 2.27 0.1552
705     py 6.7092
c
c    enclosing sphere
c
1 so 25
2 px 0
3 py 0
4 pz 0
c
c      Point source
c
```

```
5001    50 py 0.01
5002    50 py -0.01
5101    50 cy 0.15

mode p
c
c    For mixed gamma ray source, uniform spot 3mm diameter. ----
sdef cel=5100 pos=0.00001 0.00001 0.00001 erg=d1 rad=d2 ext=d3
     axs=0.32557 0.94552 0  eff 0.001
sc1  test gammas for mixed gamma source
si1  l 0.059541 0.088034 0.1220607 0.16586 0.27919 0.39170 0.66166 &
       0.89804 1.17329 1.33249 1.83605
sp1  d 1 1 1 1 1 1 1 1 1 1 1
si2  0.0 0.15
si3  -0.01 0.01
f18:p 12 22 32 42 52 62 72 82 92 102 112 122 132
      142 152 162 172 182 192 202
e18   0.0 1999i 2.0
c
m32    032000 1.
m2     007000 -.76 008000 -.24
m4     004000 1.
m6     006000 1.
m13    013000 1.
m26    026000 1.
m29    029000 1.
m42    042000 1.
m50    050000 1.
m710   071000 -0.6957 008000 -0.1420 006000 -0.1577 001000 -0.0020 007000 -0.0026
m71    071000 1.
m73    073000 1.
m82    082000 1.
m92    092235 1.
m94    094239 -0.93824 094240 -0.05974 094241 -0.00202
*tr1  0 0 0  3j    113.56 140.56 61.00    3j   1
*tr2  0 0 0  3j    112.54 141.82 119.00   3j   1
*tr3  0 0 0  3j    70.02 143.62 61.00     3j   1
*tr4  0 0 0  3j    70.79 144.13 119.00    3j   1
*tr5  0 0 0  3j    39.50 129.50 90.00     3j   1
*tr6  0 0 0  3j    31.18 100.48 61.00     3j   1
*tr7  0 0 0  3j    31.36 100.91 119.00    3j   1
*tr8  0 0 0  3j    11.50 78.50 90.00      3j   1
*tr9  0 0 0  3j    45.69 58.24 61.00      3j   1
```

```
*tr59 0.069854 0.052636 0.048481  3j   45.69 58.24 61.00     3j  1
*tr10 0 0 0  3j   44.33 58.65 119.00    3j  1
*tr60 0.14307 0.10405 -0.09696  3j   44.33 58.65 119.00    3j  1
*tr11 0 0 0  3j   63.50 26.50 90.00     3j  1
*tr61 0.044620 0.089493 0  3j   63.50 26.50 90.00     3j  1
*tr12 0 0 0  3j   89.13 29.02 61.00     3j  1
*tr62 0.003036 0.17489 0.09696  3j   89.13 29.02 61.00     3j  1
*tr13 0 0 0  3j   88.95 29.02 119.00    3j  1
*tr14 0 0 0  3j   115.20 25.20 90.00    3j  1
*tr15 0 0 0  3j   132.90 56.69 61.00    3j  1
*tr16 0 0 0  3j   132.82 56.60 119.00   3j  1
*tr17 0 0 0  3j   166.90 76.90 90.00    3j  1
*tr18 0 0 0  3j   148.92 100.22 61.00   3j  1
*tr19 0 0 0  3j   148.82 100.48 119.00  3j  1
*tr20 0 0 0  3j   142.00 128.0 90.00    3j  1
*tr50 0 0 0   19.00 109.00 90  71.00 19.00 90  90 90 0 1
nps   140000000
```

C   Future and in-progress improvements

C.1   Neutron flux

An estimate of the systematic uncertainties of the α counting measurement to determine the areal number densities of the fission deposits in the fission chamber are forthcoming.

In addition, the thickness of the fission deposits are also being measured via Rutherford backscattering of α particles. The first attempt to do this was plagued by normalization problems. This has been corrected by ordering calibrated samples from NIST. Initial results indicate that the fission deposit thickness varies by about 10% from spot-to-spot. Values averaged over the neutron beam profile are forthcoming.

C.2   Target foils

The thickness of the natural target foils will be measured as a check for variations in target thickness that have not been included.

C.3   Deadtime

Further tests are planned to try to understand event losses and to explore in-beam deadtime effects.

C.4   Internal conversion

There are two areas of investigation which will provide more accuracy and precision in α. First, follow-up calculations with the goal of calculating the O-subshell conversion coefficients will reduce the uncertainties and give us a better handle on the uncertainties in the calculations. Second, a direct measurement of α, while difficult, is feasible and may already exist somewhere. This discussion makes clear that an important consistency check will be the $8^+ \rightarrow 6^+$ transition where the uncertainty in α may even be negligible.